A FIRST EVALUATION OF ERS-1 SYNTHETIC APERTURE RADAR WAVE MODE DATA

C. BRÜNING[1], S. HASSELMANN[2], K. HASSELMANN[2], S. LEHNER[2] and T. GERLING[3]

[1] *Institut für Meereskunde, Universität Hamburg, Germany;* [2] *Max-Planck-Institut für Meteorologie, Hamburg, Germany;* [3] *Applied Physics Lab., The Johns Hopkins University, Mayland, USA*

Wave spectra extracted from 467 ERS-1 Synthetic Aperture Radar (SAR) 5×12 km wave mode imagettes obtained over the Atlantic for the three-day period 22–24 Janurary 1992 are compared with predictions of the WAM wave model (WAModel). The model was run on a $1° \times 1°$ grid and driven by the analyzed winds of the European Centre for Medium Range Weather Forecasts. Wave spectra are extracted from the imagette spectra by inverting the closed transformation relation of Hasselmann and Hasselmann that describes the nonlinear mapping of a surface wave spectrum into a SAR image spectrum. The inversion algorithm is based on the minimization of a cost function which includes a first-guess wave spectrum as a regularization term. The retrieved two-dimensional wave spectra are fully calibrated internally by the clutter spectrum, without reference to the SAR instrument calibration. The inversion scheme converged in all but 18 of the 485 imagette spectra, which passed the quality control checks applied to the original set of 494 imagette spectra.

The SAR-retrieved wave spectra show good overall agreement with the WAM wave spectra both for complex sea states and in cases in which the imaging is strongly nonlinear. Intercomparisons of the mean wavelength, mean propagation direction and directional spread show no systematic biases and only little scatter, while the SAR-retrieved significant wave heights show a similar agreement with the modeled wave heights for small and medium waves but an approximately 15% overestimation for waves larger than about 5 m. More detailed analyses using spectral correlation and multi-peak spectral partitioning techniques reveal differences for individual wave systems which can largely be attributed to deficiencies in the wind fields. Although limited to a first analysis of only a small subset of the available ERS-1 wave mode data, this first investigation demonstrates the high quality of ERS-1 SAR wave mode image spectra and the considerable potential of this data, once it has been incorporated in a general wind and wave data assimilation scheme, for improving global wind and wave forecasts.

KEY WORDS: SAR-ocean wave imaging, SAR inversion

1. INTRODUCTION

The ERS-1 Active Microwave Instrument (AMI) is a unique feature which combines a scatterometer and Synthetic Aperature Radar (SAR) operating at the same C-band frequency of 5.3 GHz (5.6 cm). In the so called 'wave mode', the AMI SAR provides approximately 5×12 km local images (imagettes) of the sea surface every 200 km along the satellite track. The power and data storage requirements for this intermittent imaging mode are sufficiently reduced for continuous, global operation to be feasible. Thus, in contrast to the full-swath SAR, which can be operated only to the exclusion of the scatterometer mode during, maximally, 10% of the orbit and while in line-of-sight of a ground station, the wave mode SAR has been operating continuously, together with the scatterometer, since the launch of ERS-1 on 16th July 1991. Data gaps exist

only during the limited periods of operation of the full-swath SAR and during occasional short periods of satellite adjustments. For the first time wave modelers are therefore obtaining, through ERS-1, continuous global information on the two-dimensional surface-wave spectrum.

However, the extraction of two-dimensional wave-spectral information from a SAR surface image spectrum is not straightforward. The SAR sees an instantaneous image of the sea surface and therefore cannot distinguish between positive and negative wave propagation directions. Multi-look analysis techniques have been proposed to resolve this ambiguity (cf. Rosenthal et al., 1989; Vachon et al., 1989), but these have not yet been implemented operationally. In addition, the imaging mechanism is strongly nonlinear due to the Doppler shifts induced by the long-wave orbital motions (velocity bunching, Larson et al., 1976; Swift and Wilson, 1979). This leads to a distortion of the SAR spectrum and a spectral cut-off beyond an azimuthal wavenumber corresponding to a wavelength of typically 100–200 m. Nevertheless, the theory of the fully nonlinear imaging of a given sea state realization into the SAR image plane is now basically well understood (Alpers et al., 1981; Hasselmann et al., 1985; Alpers and Brüning, 1986; Brüning et al., 1990) and has been successfully applied, for example, to determine the two-dimensional SAR spectrum for a given input wave spectrum using Monte Carlo Techniques (Alpers et al., 1986; Brüning et al., 1988, 1992).

More recently, the derivation of a new closed nonlinear transformation expression for the spectra themselves has enabled the spectral transformation to be computed more rapidly and accurately than with the Monte Carlo technique, making it feasible to invert the spectral mapping relation within the time constraints of operational applications (Hasselmann and Hasselmann, 1991, referred to hereafter as HH; Hasselmann et al., 1991; see also Krogstad, 1992; Bao et al., 1994). The inversion of a full day's set of ERS-1 SAR wave mode data with this method takes approximately forty minutes on a single CRAY-YMP processor. For the inversion, an approximate first-guess wave spectrum from a wave model is required to remove the 180° directional ambiguity and to augment the wave spectral information beyond the azimuthal wavenumber cut-off of the SAR.

The original ERS-1 mission plan foresaw the dissemination of the SAR wave mode Fast Delivery Product (FDP) (a smoothed imagette spectrum in polar-wavenumber coordinates) to operational users, such as the European Centre for Medium Range Weather Forecasts (ECMWF), within three hours after the satellite overpass over an ERS-1 receiving station. Operational centers were preparing to carry out the inversion routinely and to develop methods to assimilate the extracted wave spectra in wave models. Unfortunately, owing to various unforeseen software difficulties, this service only became available on February 21, 1993. However, all imagettes have been collected and archived continuously since the beginning of the mission, so that FDP products are, in principle, available prior to this time in an off-line mode.

In order to circumvent these difficulties and carry out a first evaluation of the SAR wave mode data, the authors received from ESA three days of SAR wave mode imagette data for the period January 22–24, 1992. These were Fourier transformed and smoothed to the FDP polar-wavenumber spectral format, consisting of twelve 15°

angular resolution bins and twelve logarithmically spaced wavenumber bins covering the wavelength range from approximately 100 m to 1,000 m, with an increment-to-wavenumber ratio of 0.2. The validation was carried out for the Atlantic Ocean by comparing the SAR-retrieved wave spectra against spectra computed with the third generation Wave Model 3G-WAM (or simply WAM, also referred to as the WAModel; WAMDI Group, 1988). The model was run on a $1° \times 1°$ latitude/longitude grid with $15°$ angular resolution and 25 logarithmically spaced frequencies, with an increment-to-frequency ratio of 0.1 (corresponding to a wavenumber ratio of approximately 0.2). Thus the WAModel and SAR-FDP spectral resolutions are well matched. The model was driven by surface winds from the ECMWF operational global analysis computed on a $0.56° \times 0.56°$ latitude/longitude grid. The latest operational version of the model (cycle 4) was used (Günther et al., 1992), which is based on a slightly modified input and dissipation source functions relative to the original WAModel (WAMDI Group, 1988).

The WAModel was used both to validate the SAR wave mode data and to provide the input wave spectra for the SAR inversion algorithm. In both cases the wave-model spectrum at the closest grid point and advection time (the advection time step was twelve minutes) to the location and observation time of a given SAR imagette was taken, without attempting to interpolate from several neighboring model grid points to the observation point (which introduces undesirable smoothing).

A more extensive investigation using the wave mode data from the ECMWF operational global wave model and all available SAR wave mode data for the six-month period July 1–December 31, 1992 (kindly provided off-line in the FDP format by ESTEC) has also been completed (Brüning et al., 1993). ECMWF operates the WAM cycle 4 model with the same frequency bins as used here, but with a coarser $30°$ angular resolution and on a $3° \times 3°$ grid. For the present first validation study it was considered preferable to run the WAModel with a higher spatial and angular resolution commensurate with the SAR wave mode data, and in the Atlantic, where the analyzed wind fields are more reliable than in other areas of the ocean.

A total of 494 SAR imagette spectra were obtained over the Atlantic within the model domain between $65°$ S and $65°$ N during the period Jaunary 22–24, 1992. On these nine failed to pass a signal-to-noise quality control check or were associated with insignificant wave heights. The remaining 485 spectra were subjected to the HH inversion procedure. The preliminary frequency scaling and rotation step, however, which was introduced in HH to achieve a smoother transition from the main part of the spectrum to the non-modified high-frequency region of the spectrum, was omitted to save computer time. A smoother transition can be achieved by applying a spectral partitioning method (Hasselmann et al., 1994a). The inversion method is relatively robust, the iterations converging in all but 18 of the 485 cases considered. Failure to converge was normally associated with anomalous SAR spectra which appeared to be contaminated by non-wave-like surface phenomena (slicks, wind rows, etc.). When convergence was achieved, the optimally fitted wave spectra yielded SAR spectra which agreed rather closely with the observed SAR spectra. The final fit was only weakly dependent on the details of the first-guess wave spectra within the wavenumber domain

seen by ERS-1 wave mode SAR, as required for a reliable inversion (Hasselmann et al., 1994b).

In general, the first-guess model wave spectra and the optimally fitted wave spectra derived from the SAR image spectrum agree quite well, thereby jointly validating both the WAModel and the SAR. Good agreement is found not only for typical wavelength properties, such as the peak wavelength and peak propagation direction, but also for the absolute wave heights. We note in this context that SAR image spectra yield not only relative wave spectral information, but absolutely calibrated wave height spectra. The calibration can be carried out independently of the SAR instrument calibration, and without direct cross-section measurements, using only information from the clutter background noise spectrum, which is measured simultaneously with the image spectrum (cf. Alpers and Hasselmann, 1982 and Appendix). The sea state dependence of the clutter noise level is of minor importance for the calibration. The real aperture radar (RAR) modulation transfer function (MTF) has a much stronger impact on the inversion results (Brüning, 1994). The SAR-inferred wave heights are found to be of the same accuracy (typically 10%) as radar altimeter wave heights (Hansen et al., 1994).

Apart from a small positive bias (0.22 m) in the SAR measurements of significant wave height relative to the wave model, which is incurred by an overestimate of wave heights above about 5 m, no systematic deviations between the integrated parameters of the wave model and SAR-retrieved wave spectra are found. However, discrepancies are seen in individual cases. A more detailed intercomparison of the spectral distributions using spectral pattern correlation techniques and a modified Gerling (1992) spectral partitioning scheme suggests that the deviations largely reflect inaccuracies in the wind field.

The ability of the SAR wave mode to detect possible systematic shortcomings of the wave model prediction was demonstrated by additional model integrations using 30° instead of 15° angular resolution (Brüning et al., 1993). In this case the SAR data indicated that the model underestimated the mean wavenumber, in contrast to the satisfactory prediction of this variable by the higher-resolution model.

The paper is organized as follows: the SAR model and inversion method are reviewed in Section 2. An overview of the synoptic wind and wave field situation during the three-day analysis period is given in Section 3. Section 4 shows examples of some typical intercomparisons of first-guess wave spectra, associated first-guess SAR spectra, observed SAR spectra, and optimally fitted wave and SAR spectra. Sections 5, 6 and 7 summarize the main results of this study in the form of statistical intercomparisons of the first-guess and observed SAR spectra, optimally fitted and observed SAR spectra, and first-guess and optimally fitted wave spectra. The intercomparisons are presented in Section 5 with respect to mean spectral parameters (mean wavelength, propagation direction, wave height and spectral spread), in Section 6 with respect to the pattern correlations of the spectral distributions, and in Section 7 in terms of integral parameters of individual wave systems. The final Section 8 summarizes the principal conclusions of this study. In an Appendix the clutter-noise analysis of Alpers and Hasselmann (1982), which is used to calibrate the SAR-retrieved wave spectra, is modified to accommodate the particular multi-look averaging technique implemented in the ERS-1 SAR processor (averaging over single-look image amplitudes rather than energies).

2. THE SAR SPECTRAL TRANSFORM RELATION AND ITS INVERSION

Ocean wave spectra $F(k)$ were retrieved from the SAR image spectra $P(k)$ by inversion of the following closed nonlinear transfer expression of HH (see also Hasselmann et al., 1991 and the alternative derivation of Krogstad, 1992):

$$P(k) = 2\pi^{-2} \exp\left[-k_x^2 \xi'^2\right] \int dr \, e^{-ikr} \exp\left[k_x^2 \xi'^2 \langle v^2 \rangle^{-1} f^v(r)\right]$$

$$\times \left\{1 + f^R(r) + ik_x\beta\left[f^{Rv}(r) - f^{Rv}(-r)\right]\right.$$

$$\left. + (k_x\beta)^2\left[f^{Rv}(r) - f^{Rv}(0)\right]\left[f^{Rv}(-r) - f^{Rv}(0)\right]\right\}. \tag{1}$$

Here

$$\xi'^2 = \langle \xi^2 \rangle = \beta^2 \langle v^2 \rangle = \beta^2 \int |T_k^v|^2 F(k) \, dk \tag{2}$$

represents the mean square azimuthal displacement of a scattering element in the image plane due to the Doppler shift induced by the radial component v (in the SAR look direction) of the long-wave orbital velocity; $\beta =$ slant range/SAR platform velocity; and

$$f^v(r) = \langle v(x+r)v(x) \rangle = \int F(k)|T_k^v|^2 e^{ikr} \, dk \tag{3}$$

$$f^R(r) = \langle I^R(x+r)I^R(x) \rangle$$

$$= \frac{1}{2}\int \left\{F(k)|T_k^R|^2 + F(-k)|T_{-k}^R|^2\right\} e^{ikr} \, dk \tag{4}$$

$$f^{Rv}(r) = \langle I^R(x+r)v(r) \rangle$$

$$= \frac{1}{2}\int F(k)T_k^R(T_k^v)^* + F(-k)(T_{-k}^R)^*(T_{-k}^v) e^{ikr} \, dk \tag{5}$$

denote the auto- and co-variance functions, respectively, of a the orbital velocity v and the normalized RAR (real aperture radar) cross-section $I^R(x)$. The auto- and co-variance functions are computed, cf. equations (3)–(5), as Fourier transforms of the wave spectrum $F(k)$ using the appropriate orbital velocity and RAR transfer functions T_k^v and T_k^R (cf. HH).

The orbital velocity transfer function follows from the well defined kinematics of long waves. The RAR transfer function consists of three terms, of which two, the tilt and range bunching modulation transfer functions (MTFs), are also reasonably well defined (Alpers et al., 1981; Gower, 1983), whereas the third, the hydrodynamic MTF, is not well understood theoretically and only poorly determined experimentally by relatively few, rather scattered measurements (Alpers et al., 1981; Plant et al., 1983; Hara and Plant, 1993; HH). In this model we use the hydrodynamic MTF calculated from a relaxation-time model with an estimated relaxation rate of $0.5 \, s^{-1}$ (Alpers and Hasselmann, 1978). Fortunately, the net imaging is dominated, except in the range direction, by the velocity bunching mechanism, which depends only on the well defined

orbital velocity transfer function. For ERS-1 SAR imaging of range propagating waves the geometric MTFs (tilt and range bunching modulation) in general dominate the hydrodynamic MTF (Brüning, 1994).

Apart from the nonlinear exponential factor depending on the orbital velocity correlation function, the integral (1) has the form of a Fourier transform. It can be converted into a sum of Fourier transformations by expanding this factor, yielding

$$P(\mathbf{k}) = \exp(-k_x^2 \xi'^2) \sum_{n=1}^{\infty} \sum_{m=2n-1}^{2n} (k_x \beta)^m P_{nm}(\mathbf{k}) \tag{6}$$

where the individual nonlinear spectral contributions $P_{nm}(\mathbf{k})$ can be determined by Fourier transformation (cf. HH). The complete nonlinear transformation $F(\mathbf{k}) \rightarrow P(\mathbf{k})$ can thus be rapidly computed using only fast Fourier transforms. This makes it feasible to invert the transformation using standard iterative inversion techniques based on the minimization of a suitably defined cost function.

We apply a slightly modified version of the cost function used in HH:

$$J = \int [P(\mathbf{k}) - \hat{P}(\mathbf{k})]^2 \hat{P}(\mathbf{k}) d\mathbf{k} + \mu \int \left\{ \frac{[F(\mathbf{k}) - \hat{F}(\mathbf{k})]}{[B + \min\{F(\mathbf{k}), \hat{F}(\mathbf{k})\}]} \right\}^2 d\mathbf{k} \tag{7}$$

where $\hat{F}(\mathbf{k})$ is the first-guess wave spectrum, $\hat{P}(\mathbf{k})$ the observed SAR spectrum, $P(\mathbf{k})$ the SAR spectrum computed from the best-fit wave spectrum $F(\mathbf{k})$, μ is a suitable weighting factor and $B (B = 10^{-4} \hat{F}_{max})$ is a small positive constant which prevents the denominator in the second term on the right hand side of equation (7) from becoming zero when the spectrum vanishes. The weight μ of the second term was chosen to be sufficiently small ($\mu = 10^{-3} \hat{P}_{max}^3$) so that the form of the first-guess spectrum $\hat{F}(\mathbf{k})$ no longer had a significant impact on the final solution (apart from resolving the 180° directional ambiguity and filling in the information beyond the SAR azimuthal wavenumber cut-off).

The general nonlinear variational problem

$$\delta J / \delta F(\mathbf{k}) = 0 \tag{8}$$

was solved using the iterative technique of HH based on the repeated application of the fully nonlinear forward transformation and the (explicitly solvable) quasi-linear inverse transformation.

We start from a first-guess solution, from which an improved approximate minimal-J solution is obtained. In a first step it is assumed that modifications induced in the SAR spectrum are related to modifications in the wave spectrum in accordance with the quasi-linear SAR mapping relation, defined as the lowest order term in the expansion (6) (this is identical to the linear SAR transformation expression except for the inclusion of the additional nonlinear azimuthal cut-off factor $\exp(-k_x^2 \xi'^2)$, cf. HH). The quasi-linear mapping relation generally yields an acceptable first-order approximation (at least for the present purpose of constructing an iterative minimization procedure). It has the advantage of enabling the minimization of J to be carried out explicitly in closed form. After an improved new wave spectrum has been determined using the quasi-linear mapping relations, the correct SAR spectrum associated with this new wave spectrum is then computed in a second step using the fully nonlinear mapping

relation. The procedure is repeated in the next iteration cycle using the new improved wave spectrum and associated fully nonlinear SAR spectrum as new first-guess spectra. The procedure converged in 95% of the ERS-1 SAR wave mode spectra analyzed. Adequate accuracy was normally achieved after about four to six iterations.

The two-stage technique of HH, in which the wavelength scale and mean direction of the wave spectrum were first modified without changing the shape of the spectrum before applying the above general inversion technique in a subsequent second stage, was not adopted. To reduce computing time, the general inversion technique was applied immediately to the first-guess spectrum, accepting the shortcoming that this occasionally resulted in discontinuous spectral distributions in the transition region between the low wavenumber region where the spectrum was modified by the SAR data and the high wavenumber region beyond the azimuthal wavenumber cut-off, where the lack of SAR information left the wave spectrum basically unchanged. The problems the discontinuous spectral distributions cause when assimilating SAR-retrieved wave spectra into wave models was essential. This was solved by applying a spectral partitioning method (Hasselmann et al., 1994).

The inversions were carried out in the cartesian wavenumber plane on a 128×128 grid, with a Nyquist wavenumber $k_x^{Nyq} = k_y^{Nyq} = 2\pi/32\,\mathrm{m}^{-1}$. For this purpose the FD imagette spectra were transformed from polar to cartesian coordinates. However, the SAR terms in the cost function were evaluated only in the domain for which reliable SAR data were available, i.e. in the ring $(2\pi/600)\,\mathrm{m}^{-1} \leqslant |\boldsymbol{k}| \leqslant (2\pi/100)\,\mathrm{m}^{-1}$.

The above analysis applies for noise-free SAR spectra. In practice, the SAR spectrum consists of a superposition of the wave image spectrum and the clutter spectrum (which is used to calibrate the wave image spectrum). To first order, the two spectra are simply superimposed additively without interaction (the modulation of the clutter noise by the sea is neglected) so that the clutter spectrum can be removed by subtraction. We assume that the clutter spectrum is essentially white at wavenumbers below the high wavenumber roll-off due to the system impulse response function, (Alpers and Hasselmann, 1982; Wilde et al., 1994). It can be estimated from the background spectral level at wavenumbers slightly beyond the azimuthal cut-off. In this range the clutter spectrum is still essentially white, but the wave contribution is no longer present for ERS-1 SAR imaging. For our inversions we estimated the clutter level which we subtracted from the full SAR spectrum (and used to calibrate the retrieved wave spectrum) as the average of the two FD spectral values for the highest wavenumber ($k = 2\pi/100\,\mathrm{m}$) bins in the two nearest azimuthal directions (7.5° and 172.5°).

3. THE DATA SET

3.1 SAR Wave Mode and FD Spectra

When operating in wave mode, the AMI SAR takes an approximately 5 km (azimuth) $\times$ 12 km (range) imagette of the sea surface every 200 km along the orbit (every thirty seconds). The imagettes represent three-look averages of single-look amplitude images. The imagettes must therefore be squared to yield normal SAR images defined with respect to energy. The impact of amplitude rather than energy multi-look averag-

C. BRÜNING et al.

IMAGETTE
(a)

POWER SPECTRUM
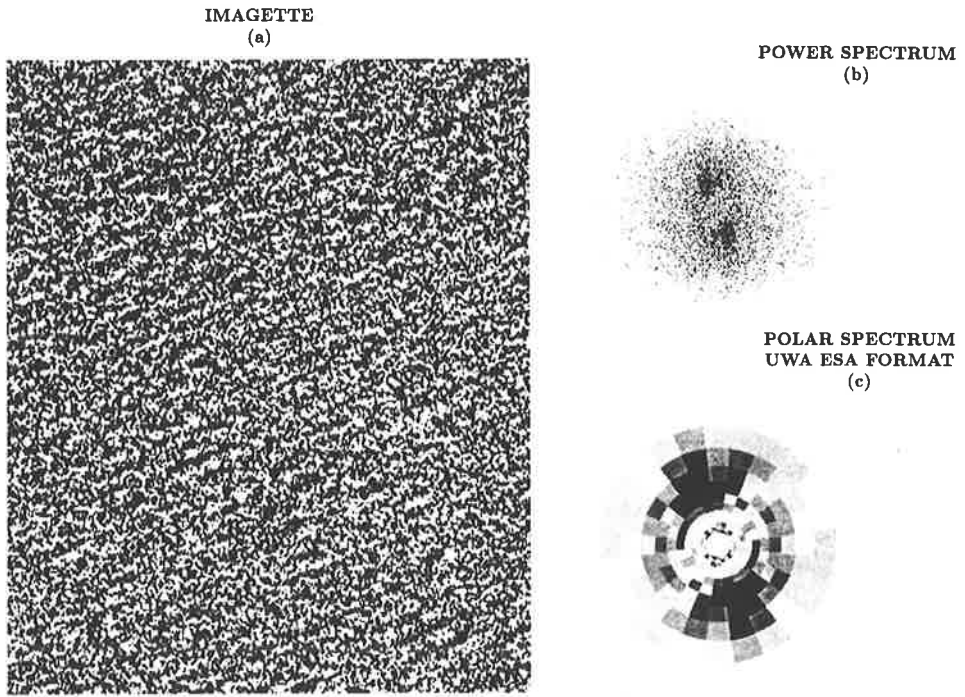(b)

POLAR SPECTRUM
UWA ESA FORMAT
(c)

FIGURE 1   ERS-1 SAR wave mode imagette (panel a) with full resolution SAR image spectrum (panel b) and fast delivery (FD) SAR spectrum (panel c).

ing on the clutter background spectrum used to calibrate the long-wave modulation spectrum is analyzed in the Appendix. The quality of the image is the same as that of the fast delivery full-swath SAR image.

The imagettes analyzed consist of 320 pixels in azimuth (flight) direction and 600 pixels in range direction, with a pixel size of the order of 16 m in azimuth and 20 m in the range direction. (In some operating conditions, the size of the imagette is smaller—320 pixels in azimuth and 400 pixels in range direction—see Figure 1). From the full imagette a 256×512 pixel sub-area (4.1×10.2 km) was chosen to compute a variance spectrum using 2D FFTs. The resulting spectrum with two degrees of freedom was then averaged to a polar-coordinate spectrum in accordance with the format of the ESA Fast Delivery (FD) product. The FD spectrum contains twelve wavelength bands spaced logarithmically between 100 m and 1,000 m, with an increment-to-wavenumber ratio of 0.2, and twelve 15° angular sectors between 0° and 180°. The area of the FD spectral bins and thus the number of degrees of freedom of the spectrum increases as the square of the wavenumber. The significance of the spectrum is therefore highest for high wavenumber and relatively low (~ 4 degrees of freedom) for the lowest wavenumber bins.

The SAR spectra occasionally exhibit spectral peaks at wavelengths of 800–1,000 m which are clearly not associated with surface waves but appeared to be related to wind

rows, slicks or other surface phenomena. To avoid contamination by these effects, and also because the number of degrees of freedom of the lowest two wavenumber bins was very low, the 800 and 1,000 m spectral bins were discarded in the inversion procedure.

A total of 494 imagettes were obtained within the model domain, (the Atlantic between 65° S and 65° N) from orbits received at Kiruna (typically ten of fourteen orbits per day) during the period January 22–24, 1992 (Figure 2). At this time the satellite was in a three day orbit repeat cycle. The data were recorded at the following UTC times:

January 22, 1992: 5:47:39–22:14:38
January 23, 1992: 5:35:01–19:58:59
January 24, 1992: 6:24:56–22:57:49

The original imagette spectra were subjected to quality-control checks which rejected spectra if the signal-to-noise ratios were too low (ratio of peak spectral energy to background spectrum less than 3 dB: 5 spectra) or if the wave heights were regarded
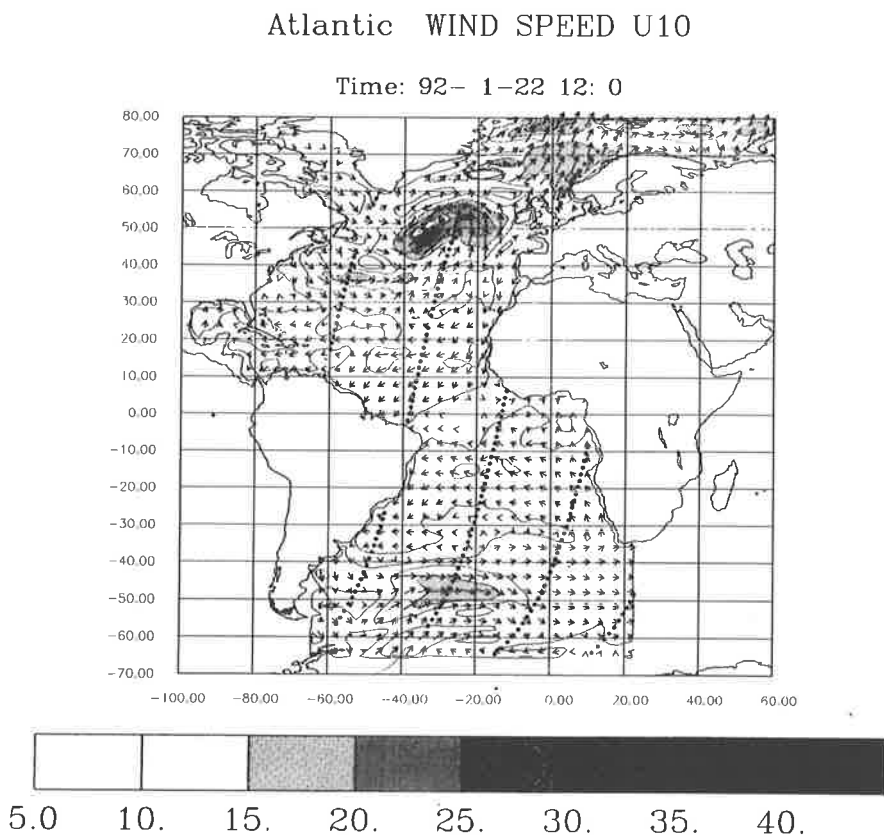
FIGURE 2   Wind fields over the Atlantic at 12 UTC on the 22nd (panel a) and 24th (panel b) of January, 1992, together with locations of imagettes. Arrows indicate the magnitude (also depicted by isolines) and direction of the wind vector. (see color plate II at the end of this issue).

C. BRÜNING et al.

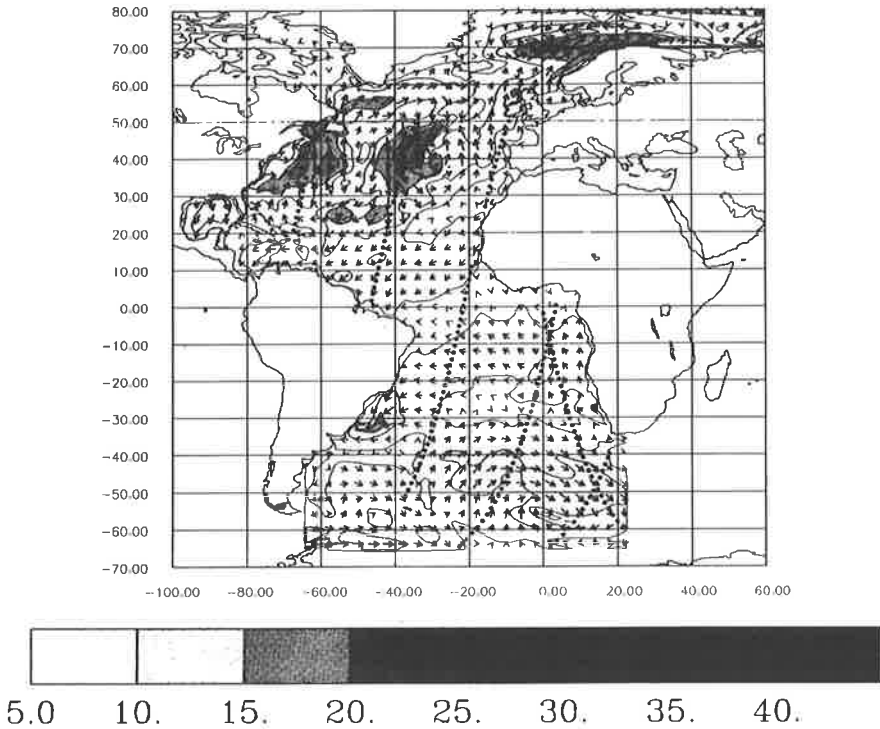# Atlantic WIND SPEED U10

Time: 92– 1–24 12: 0

FIGURE 2 (*continued*)

as insignificant (less than 0.5 m: 4 spectra). The remaining 485 quality-controlled imagette spectra were then inverted, the inversion converging in 467 cases.

3.2 The Synoptic Situation

Figures 2a, b show the wind velocity field (10 m height) over the Atlantic on the 22nd and 24th of January at 12 UTC, together with the locations of the imagettes obtained on these days. On the 22nd, a high-wind region is located north of the Norwegian coast with north-easterly wind speeds up to 25 m/s, a stronger storm is centered at 50° N latitude with north-easterly winds up to 35 m/s, and there is a further high-wind region at 45° S in the South Atlantic with easterly winds up to 20 m/s. During the next three days, the storm in the South Atlantic abates, while the storm in the North Atlantic moves to the north-east, reaching the Scottish coast on January 23. This is followed by new storm systems in the 35°–40° N latitude belt with wind speeds up to 30 m/s.

The resulting wave fields computed with the WAModel for the 22nd and 24th of January are shown in Figures 3a, b. On January 22, the highest waves with a significant

wave height of 11 m are found propagating eastward in the North Atlantic storm, while high waves of up to 8 m are seen propagating north-eastward north of Norway and eastward in the South Atlantic. During the following days, the wind abates in the south and an eastward propagating swell system with significant wave heights of up to 6 m has developed at about 50° South. In the North, the three consecutive storms produce windseas with up to 10 m significant wave height.

4. EXAMPLES OF SAR MAPPING AND INVERSION

The interrelationship between observed SAR spectra, modeled first-guess wave spectra, the associated (computed) first-guess SAR spectra and SAR-retrieved wave spectra is illustrated in this section for two sequences of wavenumber spectra obtained along two separate orbits (Figures 4, 5). The sequences were selected to illustrate different sea states. They include single and multiple peaked spectra consisting of various combina-
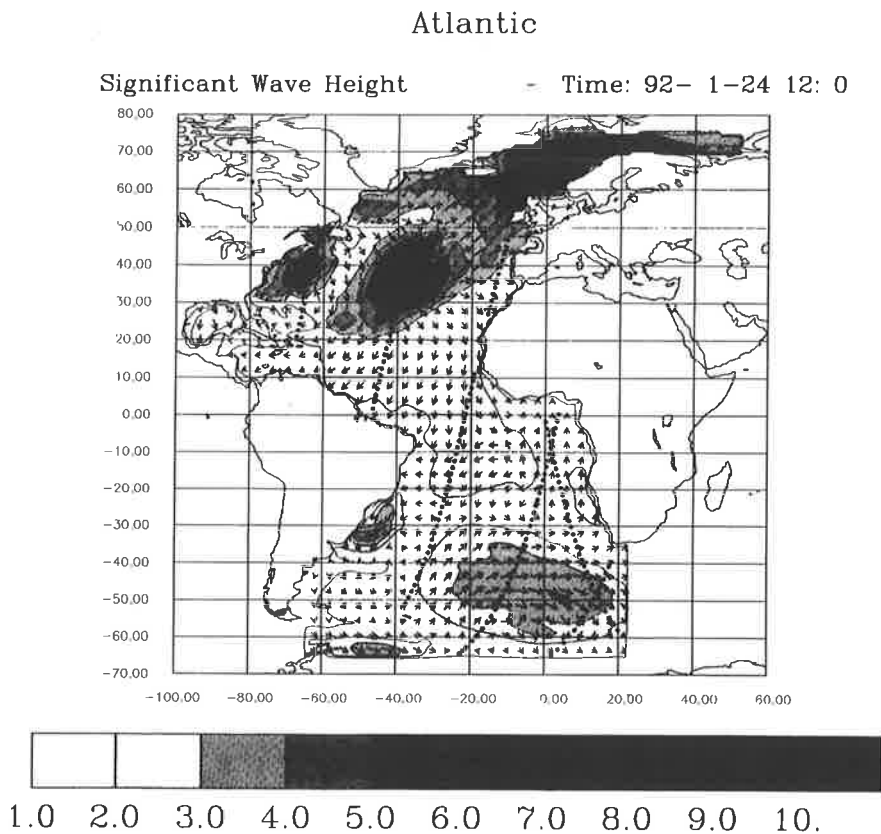

FIGURE 3   Same as Figure 2 for significant heights and mean wave propagation directions. (see color plate III at the end of this issue).

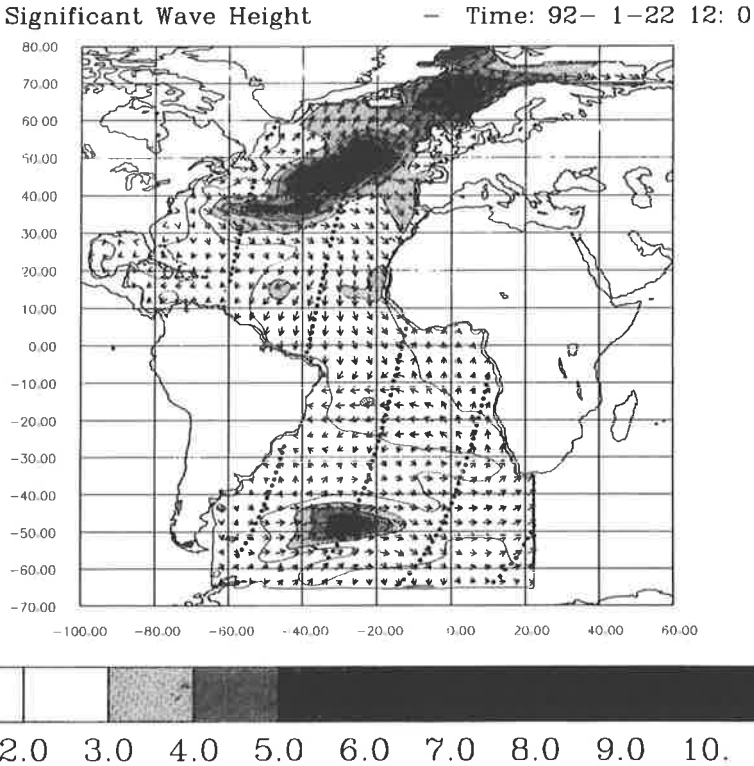C. BRÜNING et al.

Atlantic

FIGURE 3   (Continued).

tions of windsea and swell components, weakly and strongly nonlinear mapping conditions, and azimuthal and range propagating waves.

In Figures 4 and 5, each row (i), (ii),... represents one intercomparison sequence, consisting of five panels (a)–(e). Panel (a) shows the first-guess wave spectrum from the WAModel; panel (b) the first-guess SAR spectrum computed from the first-guess wave spectrum of panel (a) by applying the forward closed integral transformation (equation 1); panel (c) the best estimate wave spectrum obtained by inverting the measured SAR spectrum; panel (d) the best estimate SAR model spectrum calculated from the wave spectrum of panel (c); and panel (e) the observed ERS-1 SAR wave mode image spectrum. The spectra are shown for the domain $k_x \leqslant 2\pi/128 \, \mathrm{m}^{-1}$, $k_y \leqslant 2\pi/128 \, \mathrm{m}^{-1}$ in which most of the SAR information was available (outside the square $k_x = k_y \geqslant 2\pi/100 \, \mathrm{m}^{-1}$ the SAR-retrieved spectra revert to the first-guess spectra). If the inversion is successful, panels (d) and (e) should be very similar—as indeed they are. Although many of the wave spectra are rather complex, exhibiting three or four different wave systems, the general structures of the modeled and SAR-retrieved wave spectra normally agree remarkably well. However, due to the nonlinearity of the
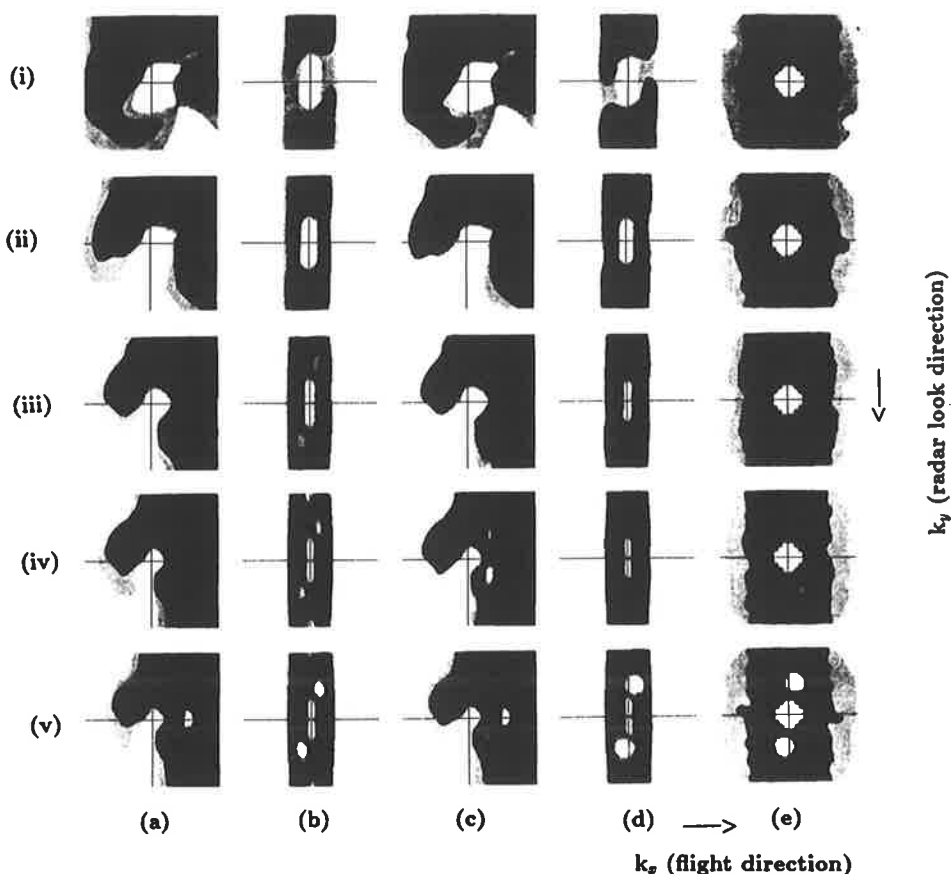
FIGURE 4 Sequence of spectra obtained on January 24, 1992 between 13:13–13:15 UTC along a 1,000 km pass over the North Atlantic (49.6°–42.6° N; 325.5°–323.3° E). Panel (a) first-guess wave spectra; panel (b) simulated first-guess SAR spectra calculated from (a); panel (c) optimally fitted wave spectra; panel (d) optimally simulated SAR image spectra calculated from (c); panel (e) ERS-1 SAR wave mode image spectra. Spectra are plotted on a logarithmic scale with 4 dB isoline spacing for the wave spectra (panel a, c) and 1 dB for SAR spectra (panels b, d, and e). (see color plate IV at the end of this issue).

imaging mechanism, the SAR spectra prior to inversion show relatively littel similarity with the modeled wave spectra.

The first sequence (Figure 4), obtained on a descending pass on 24 January 1992, 13:13–13:18 UTC over the North Atlantic (49.6°–42.6° N; 325.5°–323.3° E) is of interest because the satellite crosses a storm center, with maximum significant wave heights of 10 m. The first-guess model wave spectrum at the northern end of the pass (Figure 4 (i), panel a) shows a trimodal wave system whose main component propagates in range direction, with two secondary wave systems propagating in azimuthal direction. The significant wave height is 3 m. The SAR-retrieved wave spectra confirm these three wave systems (Figure 4 (i), panel c), but with slightly different weigting of the individual wave systems. As the satellite proceeds southwards, the azimuthal wave
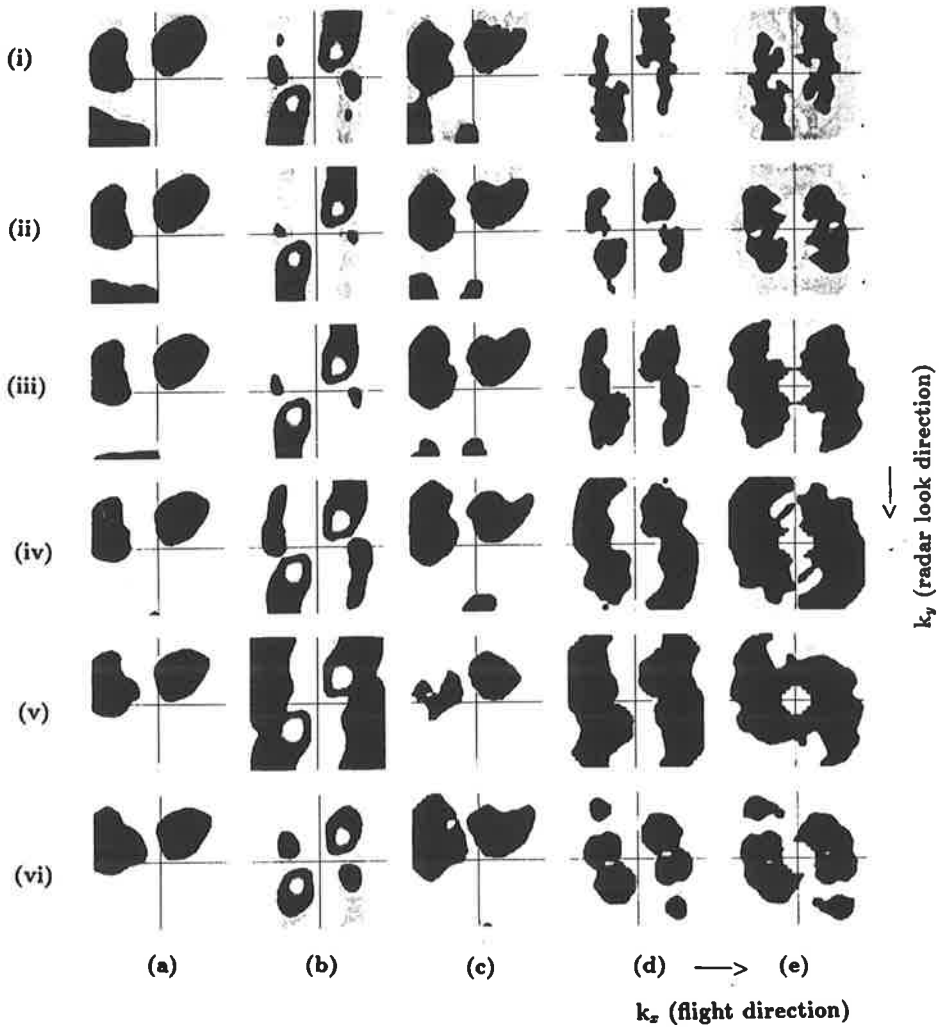
FIGURE 5 Same as Figure 4, for spectra obtained on Januray 24, 1992 along a 1,200 km pass between 10:12–10:15 UTC over the South Atlantic (21.0°–29.9° S; 358.6°–356.0° E). (see color plate V at the end of this issue).

system becomes more pronounced and the wave heights increase. The model wave spectrum (Figure 4 (iii), (iv), $\cdots$; panels a) develops a broad windsea component with a significant wave height of order 7–8 m propagating in azimuthal direction. Under these conditions the SAR mapping can be expected to be highly nonlinear, as is indeed seen: both the computed first-guess SAR spectra (panel b) and the measured ERS-1 SAR spectra (panels e) are strongly distorted relative to the wave spectra (evident especially in the strong azimuthal cut-off and the multiple peaks). However, realistic wave spectra are successfully recovered even from these highly nonlinear cases, as demonstrated by the close fit of the optimally fitted and measured SAR spectra (panels

d and e) and the reasonably good agreement between the first-guess and SAR-retrieved wave spectra (panels a and c).

The measured ERS-1 spectra (panel e) often exhibit a somewhat higher back-ground noise level than the optimally fitted SAR spectra (panel d) beyond the azimuthal cut-off wavenumber. This may be due to the fact that clutter noise, which was estimated from the two highest wavenumber bins in the azimuthal directions and subtracted from the FD SAR spectrum, is not perfectly white, as assumed (see state dependence, system response function fall off, antenna pattern influence). Another frequent discrepancy is a stronger simulated azimuthal cut-off than observed, especially for high sea states. This may be in part due to the transformation of the high resolution imagette spectra into the coarse polar FD spectra by which the energy is smeared out.

The next sequence (Figure 5(i)–(iv)) shows a complex sea state, imaged on a descending orbit on 24 January 1992 between 10:12–10:15 over the South Atlantic (21.0°– 29.9° S; 358.5°–356.0° E). The wave spectra exhibit bimodal and trimodal wave systems propagating in both azimuth and range directions. In these cases the peak energy densities of the simulated first-guess SAR spectra panels b) are higher than the measured ERS-1 SAR wave mode spectra (panels e), indicating an overestimate of the first-guess wave spectra (panels a). Apart from this adjustment, however, the first-guess wave spectra are in reasonable agreement with SAR-retrieved wave spectra (panels c), although shifts of the spectral peak as well as changes of the energy level of individual wave components can be clearly identified. The third wave system propagating in a range direction dies out in the model sequence (panels a) as the satellite proceeds southwards, but is still visible on the SAR-retrieved wave spectra (panel c). This could point to deficiencies of the analyzed wind fields in the South Atlantic.

A more comprehensive intercomparison of the principal spectral properties of the model first-guess and SAR-retrieved wave spectra for the complete set of Atlantic data is presented in the following two sections.

5. STATISTICAL INTERCOMPARISON OF MEAN SPECTRAL PROPERTIES

Figures 6 to 9 show the intercomparison scatter diagrams of significant wave height, mean wavenumber, mean propagation direction (measured clockwise relative to the flight direction at $\phi = 0°$), and directional spread (as defined in Yamartino, 1984), respectively, for the model first-guess wave spectra and the SAR derived spectra for the 467 computed inversions. The SAR-retrieved significant wave heights tend to be larger than the model wave heights for higher wave heights, resulting in a mean bias of $+ 0.22$ m and a regression line slope of 1.12 (the regression line is defined symmetrically and is restricted to pass through zero, as in Bauer et al., 1992). Figures 10 and 11 show a similar comparison of the mean wavenumbers and mean directions for the computed first-guess observed SAR spectra. The distribution of the mean wavenumbers is non-uniform. The mean wavenumbers of the observed SAR spectra tend to be larger than the first guess wavenumbers. This is partly due to the smoothing caused by the transformation of the high resolution imagette spectra into the coarse FD spectra.

Significant waveheight   90 N – 90 N   0 E 360 E   Jan. 1992

WAM   2.539   ERS 1   2.765   Stdev   0.461   Scatter   0.185   Slope   1.117   Correl   0.977   No.   462
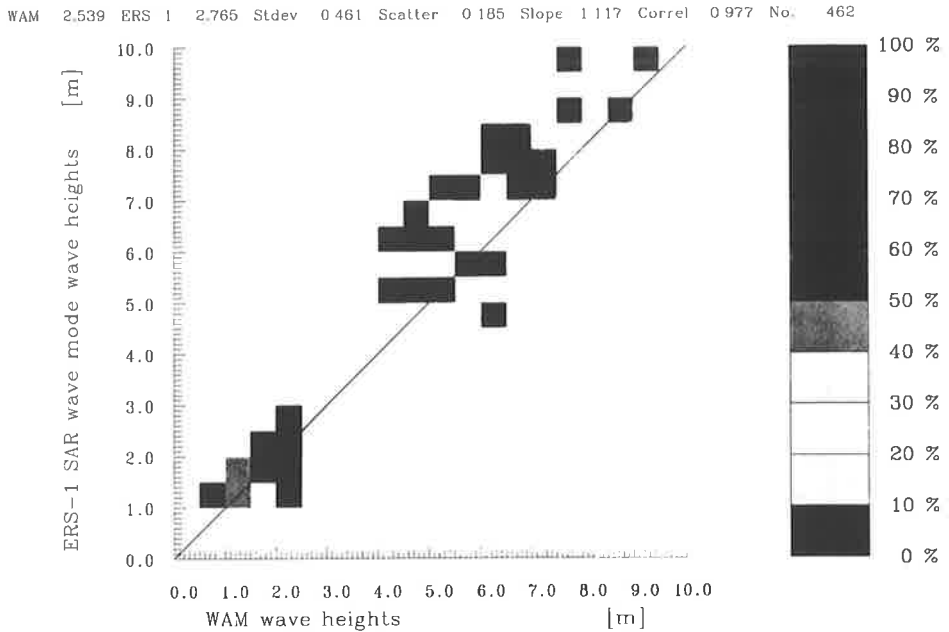

FIGURE 6   Comparison of modeled and SAR-retrieved significant wave heights for spectra obtained during the period January 22–24, 1992 over the Atlantic. Each colorbar includes 10% of the 462 entries. (see color plate VI at the end of this issue).
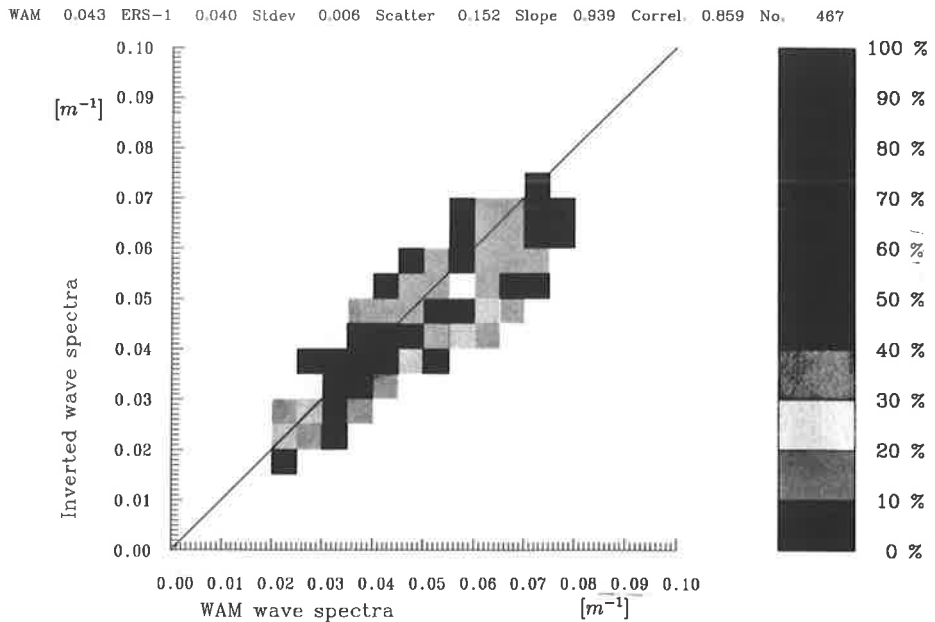
Mean wavenumber   90 N – 90 N   0 E 360 E   Jan. 1992

WAM   0.043   ERS–1   0.040   Stdev   0.006   Scatter   0.152   Slope   0.939   Correl   0.859   No.   467

FIGURE 7   Same data set as Figure 6 for mean wavenumbers, 467 entries. (see color plate VII at the end of this issue).

Mean direction   90 N −90 N   0 E 360 E   Jan. 1992

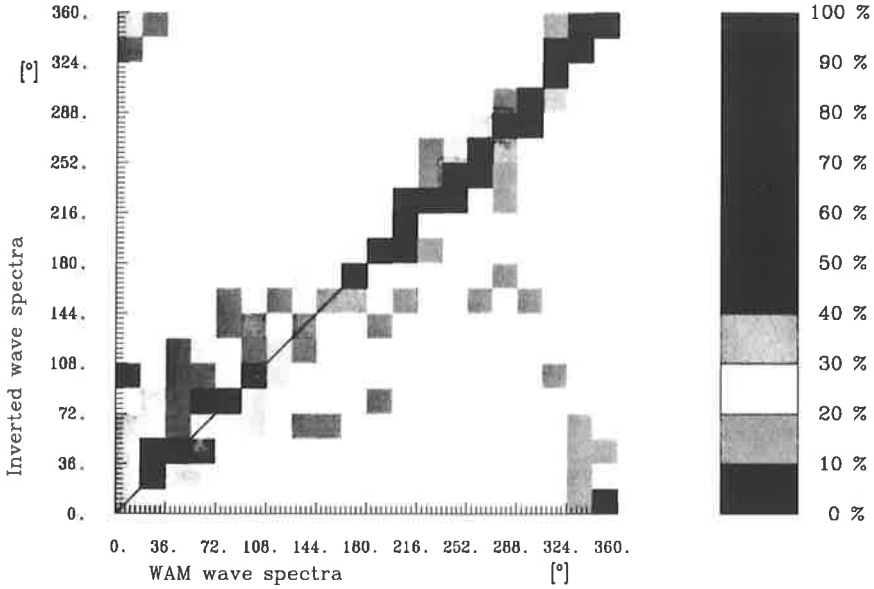WAM 201.690 ERS−1 193.503 Stdev 72.885 Scatter 0.379 Slope 0.962 Correl. 0.752 No. 467

FIGURE 8   Same data set as Figure 6 for mean directions, 467 entries. (see color plate VIII at the end of this issue).

Spreading   90 N −90 N   0 E 360 E   Jan. 1992

WAM 0.959 ERS−1 0.937 Stdev 0.119 Scatter 0.129 Slope 0.975 Correl. 0.945 No. 467
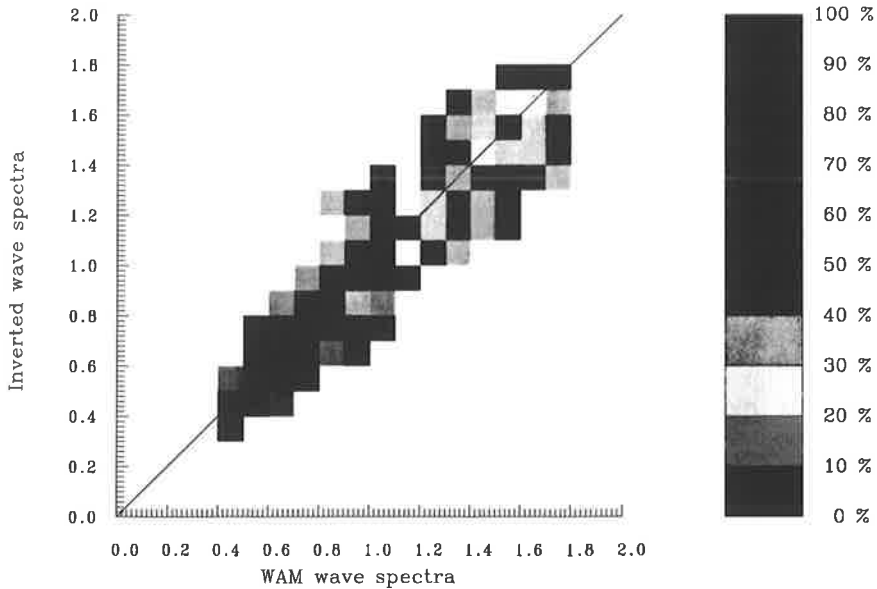

FIGURE 9   Same data set as Figure 6 for directional spread, 467 entries. (see color plate VIV at the end of this issue).

C. BRÜNING et al.

Mean wavenumber   90 N --90 N   0 E 360 E   Jan. 1992

WAM 0.027 ERS-1 0.031 Stdev 0.007 Scatter 0.264 Slope 1.099 Correl 0.418 No. 467
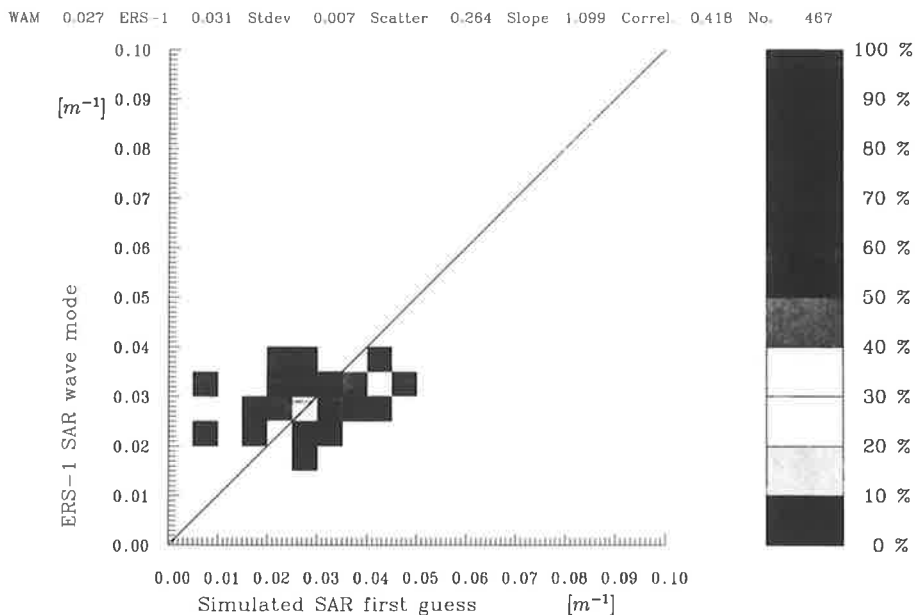

FIGURE 10   Comparison of mean wavenumbers, computed for the simulated first-guess SAR spectra and for the ERS-1 SAR wave mode image spectra; same data set as Figure 6, 467 entries. (see color plate X at the end of this issue).

Mean direction   90 N --90 N   0 E 360 E   Jan. 1992

WAM 96.115 ERS-1 93.734 Stdev 11.323 Scatter 0.123 Slope 0.969 Correl 0.749 No. 467
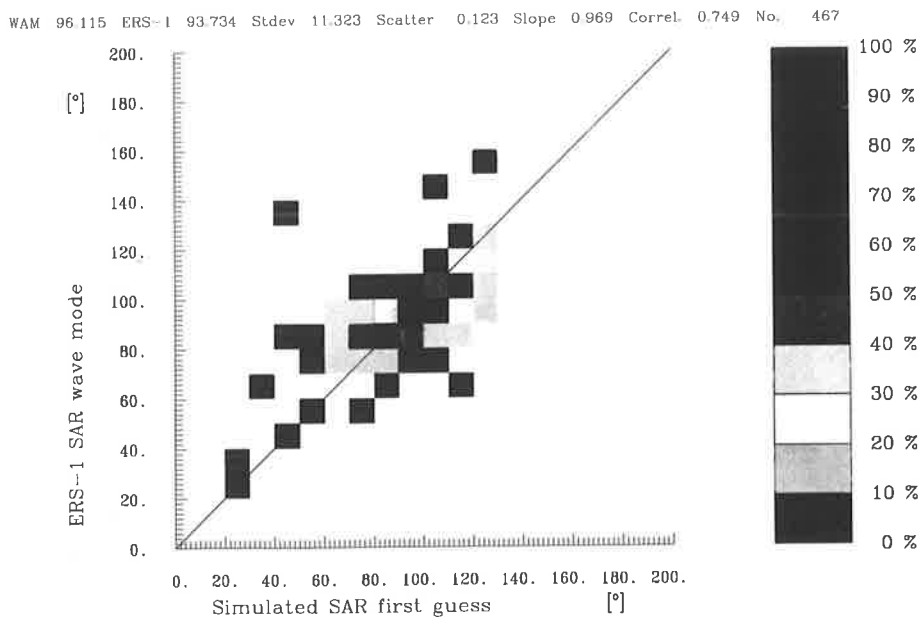

FIGURE 11   Same as Figure 10 for mean directions, 467 entries. (see color plate XI at the end of this issue).

Another, more important, reason is that in about 35% of the measured SAR spectra, peak wavelengths of the order of 800–1,000 m are found which, as mentioned above, have no counterpart in the first-guess wave field and appear to be associated with surface phenomena other than waves.

The distributions of the mean directions of the computed first-guess SAR spectra and the observed SAR spectra (Figure 11) are non-uniform and suggest a bias of the observed SAR spectra towards the 90° (range) direction. The non-uniformity could perhaps be explained by the small number of meteorological situations encountered in the relative brief three-day analysis period. However, the bias towards the range direction could be an indication of an inaccurate representation of the hydrodynamic modulation transfer function. To investigate this question further, one could optimize the hydrodynamic MTF by treating it as an undetermined free function in the minimization of the source function.

After the wave spectra have been optimally fitted, the mean wavenumbers and directions of the associated SAR spectra agree very closely with the observed SAR spectra, as expected (Figures 12, 13). However, the bias of the observed SAR spectra towards small wavenumbers and the non-uniform distribution is not removed, since the very low wavenumber non-wave features and the different cut-off levels responsible for the bias cannot be explained and removed by a realistic modification of the wave spectrum.

Mean wavenumber   90 N –90 N   0 E 360 E   Jan. 1992

WAM   0.026 ERS–1   0.031 Stdev   0.008 Scatter   0.311 Slope 1.143 Correl. 0.399 No.   467
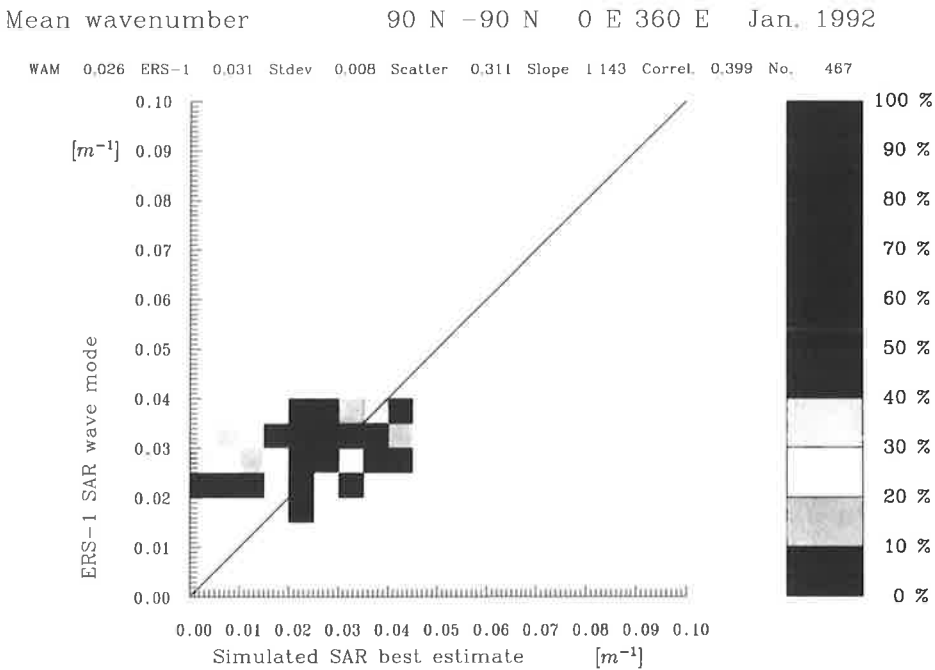
FIGURE 12   Same data set as Figure 6; comparison of mean wavenumbers, for the optimally fitted SAR spectra and for ERS-1 SAR wave mode image spectra, 467 entries. (see color plate XII at the end of this issue).

Mean direction   90 N −90 N   0 E 360 E   Jan. 1992

WAM 94.393 ERS−1 93.734 Stdev   7.098 Scatter   0.076 Slope 0.990 Correl. 0.877 No.   467
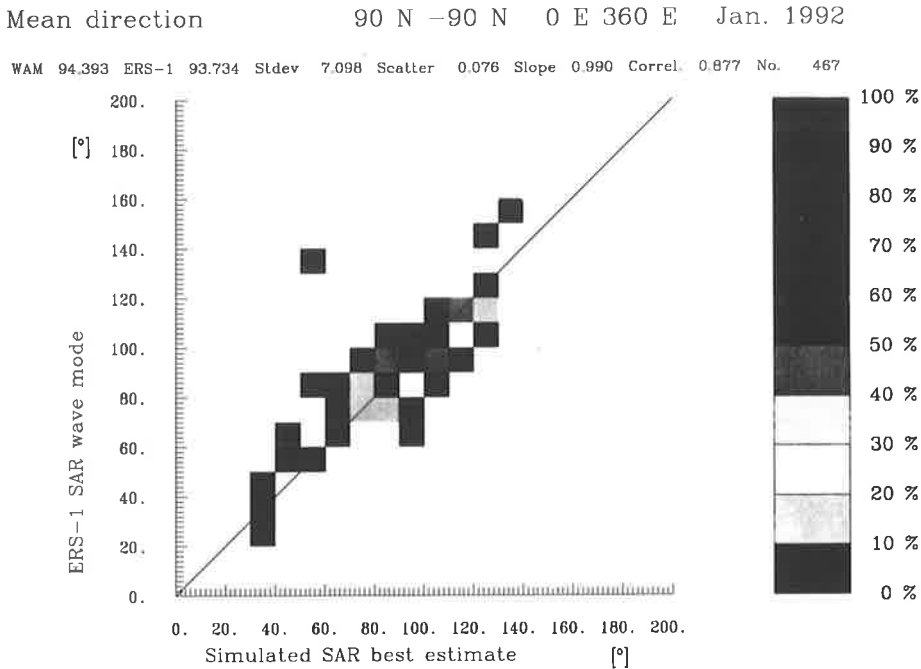

FIGURE 13   Same data set as Figure 6; computed as Figure 12 for mean directions, 467 entries. (see color plate XIII at the end of this issue).

6. SPECTRAL CORRELATIONS

The spectral distributions of the modeled and SAR-retrieved wave spectra cannot be adequtely compared in terms of only a few integral parameters. In the next section, we therefore consider a generalization of the analysis of the previous section to a larger number of characteristic spectral parameters. Nevertheless, the similarity of two spectral distributions can be characterized in terms of a single index, the spectral pattern correlation. The correlation index, presented in the following two sub-sections, is useful in determining whether or not two spectral distributions agree. However, it is unable to identify the nature of possible discrepancies, for which the more detailed analysis technique of the next section must be applied.

6.1 Pattern Correlation of WAM and Inverted SAR Wave Spectra

The degree of similarity between the two-dimensional WAM and SAR-retrieved wave spectra S_{WAM} and S_{SAR}, respectively, may be characterized by the pattern correlation coefficient

$$K = \frac{\int\int S_{WAM}(f,\Theta) S_{SAR}(f,\Theta) df d\Theta}{\left[\int\int S_{WAM}^2(f,\Theta) df d\Theta \int\int S_{SAR}^2(f,\Theta) df d\Theta\right]^{1/2}} \qquad (9)$$
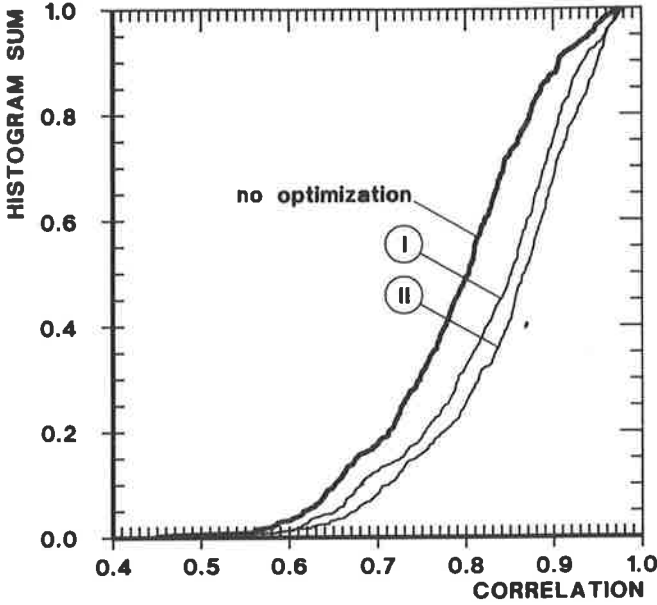
FIGURE 14   Histograms of spectral pattern coefficients for modeled and SAR-retrieved wave spectra for: no optimization (no sysmbol); optimally rotated SAR-retrieved wave spectra in accordance with problem 1 (I) and; optimally rotated and frequency scaled SAR-retrieved wave spectra in accordance with problem 2 (II).

Figure 14 (a, solid line) shows the histogram sum of K for the 467 spectra taken over the Atlantic. The correlation coefficients are seen to be higher than 0.65 in about 90% of the cases and higher than 0.8 in about 50% of the cases. The mean correlation coefficient is $\bar{K} = 0.79$, with a standard deviation of 0.096. For spectra north of the equator, the mean correlation $\bar{K}_N = 0.815$ is slightly higher than for spectra south of the equator, $\bar{K}_S = 0.76$.

6.2 Maximized Pattern Correlations through Rotation and Frequency Scaling

It is of interest to determine the extent to which the difference between the spectral distribution of the modeled and SAR-retrieved wave spectra can be attributed simply to errors in the mean propagation direction and the frequency scale. To investigate this question, optimized directional turning and frequency rescaling parameters $\Delta\Theta$ and α, respectively, were determined by solving the least square problems

$$\text{I} \quad J_1(\Delta\Theta) = \int [S_{WAM}(f, \Theta) - S_{SAR}(f, \Theta - \Delta\Theta)]^2 \, df \, d\Theta \doteq \min$$

$$\text{II} \quad J_2(\alpha, \Delta\Theta) = \int [S_{WAM}(f, \Theta) - S_{SAR}(\alpha f, \Theta - \Delta\Theta)]^2 \, df \, d\Theta \doteq \min$$

for $\Delta\Theta$ (problem I) and for $\Delta\Theta$ and α (problem II).

The histogram sum of the solutions $\Delta\Theta$ for problems I and II for the 467 spectra are shown in Figure 15. The differences between I and II are minimal; i.e. there is little coupling between directional and frequency tuning. The associated histogram sum of the frequency scaling parameter α for problem II is plotted in Figure 16. The mean value of $\Delta\Theta$ is 1.0° (for both problems I and II), with a standard deviation of 7.5°, while the mean value of α (problem II) is 1.03, with a standard deviation of 0.09. The corresponding histogram sum of the pattern correlations after optimal rotation (problem I) and after optimal rotation and frequency rescaling (problem II) are shown in Figure 14. The mean value for the optimized correlation K_{opt} increases from $K = 0.79$ to $K_{opt} = 0.847$, with a standard deviation of 0.09. The percentage of cases with a pattern correlation greater than 0.8 increases from the original value of 50% to 75% after optimization. We conclude that a significant increase in the pattern correlation can be achieved by a straightforward rotation and rescaling correction. This correction will presumably be effective mostly for single-peaked spectra, and will often fail for multi-peaked distributions.

The geographical distribution of the correlations is shown in Figure 17. The length of the line to the left of the imagette is proportional to $(1 - K)$, while the length of the line to the right is proportional to $(1 - K_{opt})$. The correlation is found to be highest for spectra dominated by one strong peak in the northern and southern storm areas and is lowest for multi-peaked spectra, as expected.
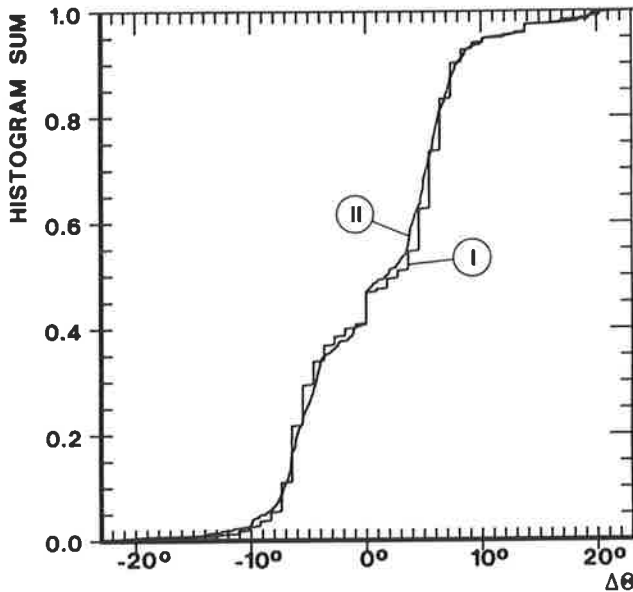

FIGURE 15   Histogram sums of optimally fitted angular turning parameters $\Delta\Theta$ for problem I (only $\Delta\Theta$ fitted) and problem II (simultaneous fits of $\Delta\Theta$ and frequency scaling factor α).
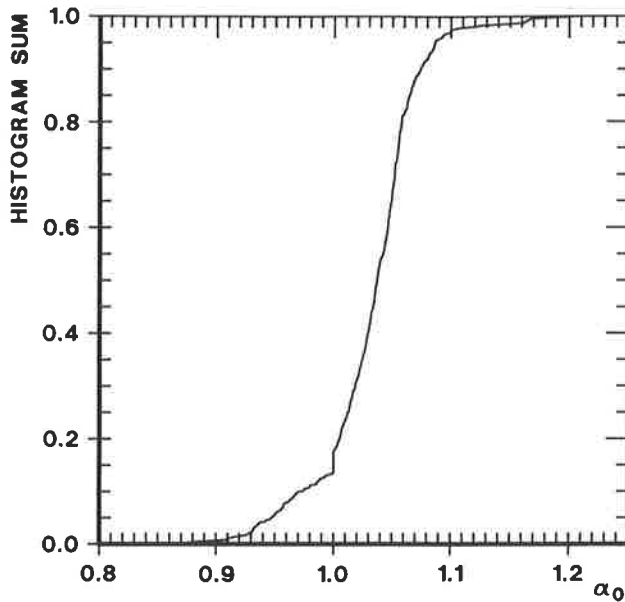
FIGURE 16   Histogram sums of optimally fitted frequency scaling parameter α for problem II (simultaneous fits of $\Delta\Theta$ and α).

7. SPECTRAL PARTITIONING

A more detailed intercomparison of the modeled and SAR-retrieved wave spectra requires an analysis of the space-time evolution of the spectral distributions. However, this is difficult to depict in practice for the full spectral representations because of the very large quantities of data involved. The statistical intercomparisons in Section 5 of mean wave height, wavelength, propagation direction and directional spread represent a useful projection onto mean sea state properties, but fail to capture important features of the spectrum, particularly when the wave spectrum—as is usually the case—is composed of a number of different windsea and swell systems. A useful compromise between the full spectral representation and the mean-parameter approach has recently been proposed by Gerling (1992). The basic idea is to decompose the wave spectrum into a number of separate wave systems, each of which can then be characterized by its individual set of standard mean spectral parameters.

Gerling's original partitioning scheme was slightly modified in the present application by defining the wave systems as 'inverse catchment areas'. In hydrology, a catchment area (watershed) is defined as the set of all points of a topographic terrain which drain into the same local topographic minimum. Similarly, we assign a 'peak region' to a local spectral peak by inverting the spectral topography, so that the spectral peak becomes a local minimum, and defining the 'peak region' as the catchment area of this local minimum. Expressed directly, a 'peak region' is the set of all spectral points whose paths of steepset ascent lead to the same spectral
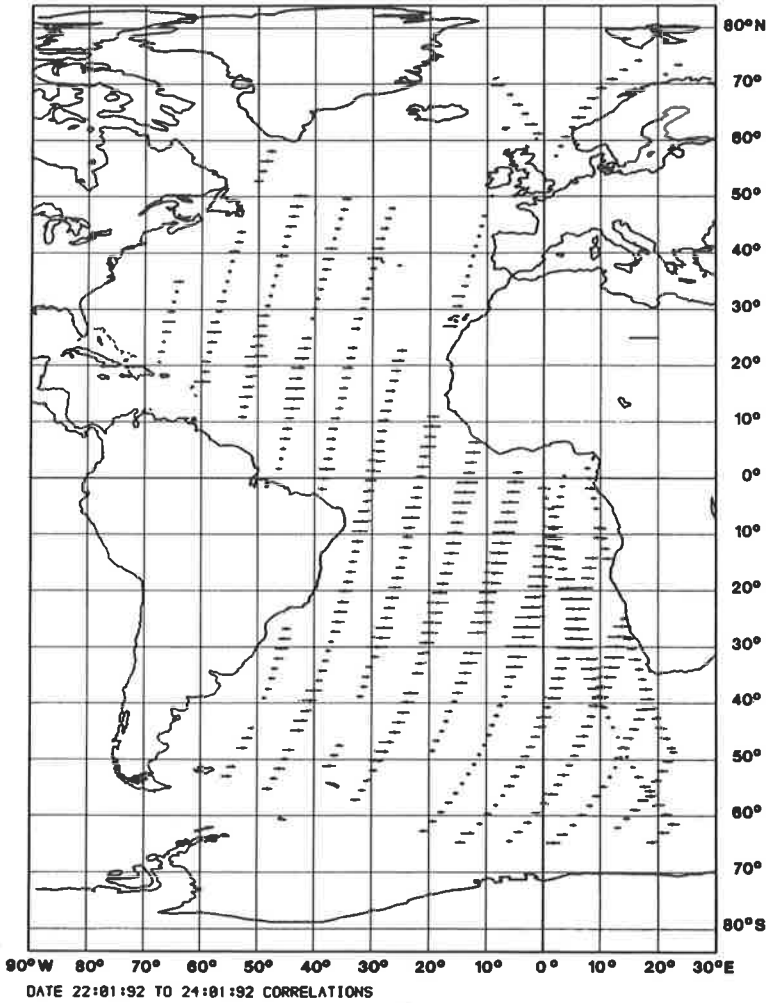
ERS1   WAVE MODE

FIGURE 17 Geophysical distribution of 'pattern correlation deficit' $(1 - K)$ (left bar) for original SAR-retrieved spectra and $(1 - K_{opt})$ (right bar) for SAR-retrieved wave spectra after optimal rotation and frequency rescaling.

peak. The path of steepest ascent is defined here as the set of directed path segments which connect any given grid point to the highest of its four nearest-neighbor grid points.

In practice, the scheme must be augmented by additional conditions for coalescing neighboring peak regions when their separations are not statistically significant. In addition, to comparing spectra at different locations and times, or from different data sources (e.g. first-guess wave spectra versus SAR derived wave spectra) algorithms for

identifying and cross-assigning wave systems, i.e. for deciding whether wave systems of different spectra represent the same wave system, must be developed. In general this can become rather intricate, but in the cases considered here, the identification was generally relatively straightforward.

The spectral partitioning scheme was applied to three successive orbits:

pass 1: January 24, 1992; 10:06–10:24 UTC; 37 spectra
pass 2: January 24, 1992; 11:33–12:01 UTC; 49 spectra
pass 3: January 24, 1992; 13:13–13:24 UTC; 27 spectra

In this set of 113 spectra, seven separate wave systems were identified.

The significant wave height, mean wavelength and propagating directions of the partitioned wave systems for the first-guess WAM wave spectra (panels a) and for the SAR-retrieved wave spectra (panels b) are shown in Figure 18 (significant wave height) and in Figure 19 (mean wavelength). The overall agreement is surprisingly good, the same wave systems appearing with characteristics in both data sets.

Several of the wave systems have large spatial extents and are observed in two or all three passes. The wave system 1 (Figures 18, 19) originates in the North Atlantic storm systems off the east coast of North America and propagates along a great-circle path into the South Atlantic. It is clearly seen in all three passes. The wave system 2 was generated by South Atlantic storms and is confined to the South Atlantic basin. It is seen only in passes 1 and 2. Systems 3 and 4 were generated by the southern and northern trade winds, respectively. Swell from system 3 can be traced into the North Atlantic. The remaining systems 5, 6, and 7 represent local windseas and are of more limited extent.

Despite the good overall agreement between the first-guess and SAR-derived spectra, small systematic differences between the WAM and SAR-retrieved partitioning parameters can be seen for individual wave systems. These become more apparent when the parameters are plotted as functions of latitude along an orbit pass. The differences can be used to identify errors in the wind field driving the WAModel, in the WAModel itself, or in the SAR imaging model (in particular, in the hydrodynamic modulation transfer function).

Figures 20 and 21 show an intercomparison of WAM and SAR-retrieved significant wave heights (panels a) and wavelengths (panels b) for the wave systems 1 and 2 as a function of latitude along the orbits 1 and 3, respectively.

System 1 appears in both orbits (and also in the intermediate orbit 2, not shown). The SAR data suggests that the model may have missed some peaks associated with unresolved local high winds in the source region around 33° N and 40° N (orbit 3 Figure 21a). The model also appears to be overstimating the swell radiating from the system 1 storm in the latitude band around 10°–30° S (orbit 1, Figure 20a). The modeled and SAR-retrieved wavelengths agree relatively well, with the exception of some high noise values in the SAR data (Figures 20b, 21b) which could probably be explained by non-wave-like features in the SAR images, as discussed above.

The wave system 2 is shown here only for orbit 1 (Figure 20), although the system is also found in orbit 2. Compared with wave system 1, the wave heights in the source region are lower and the wavelengths correspondingly shorter. The agreement is satisfactory also in this case, although there is again an indication that the model may

have missed a region of higher winds in the generating region around 50° S (Figure 20a). There is also some indication of noise in the SAR wavelength data around 10° S.

In summary, the examples show good general agreement between the SAR-retrieved and modeled spectral partitioning parameters, but also sufficient differences to demonstrate the potential improvements in wind field analyses—in particular in regions of rapidly changing high winds—which could be attainable with a combined wind and wave data assimilation scheme which makes full use of the information contained in the SAR data.
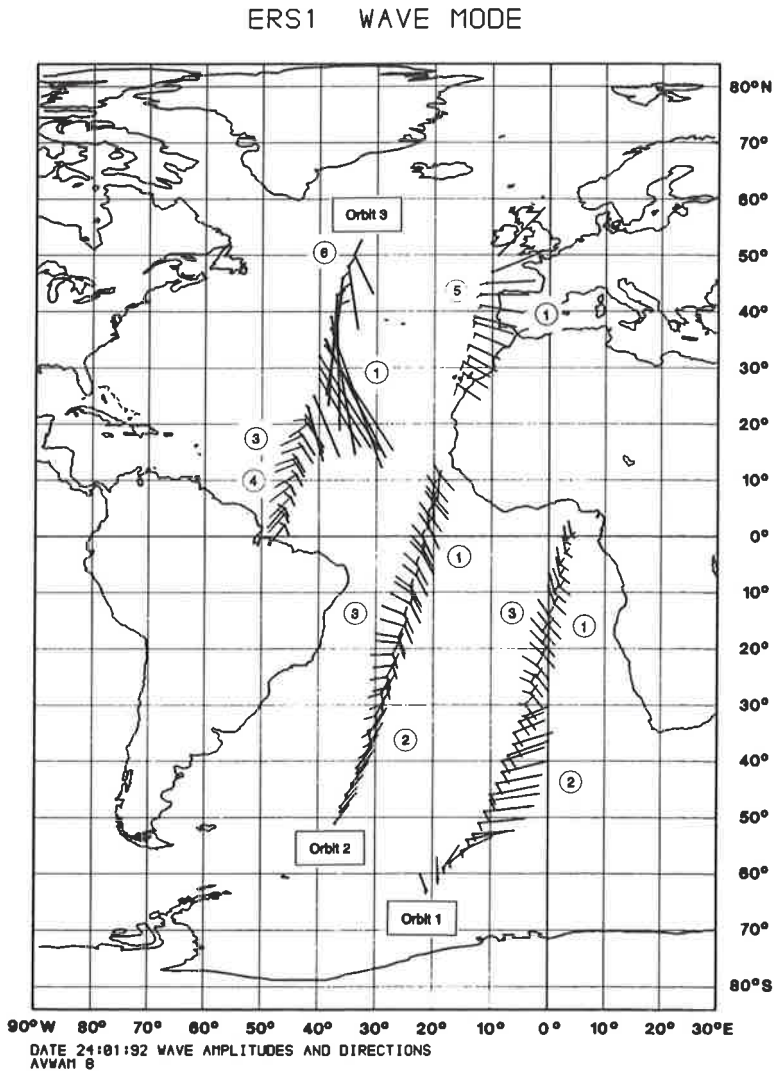

FIGURE 18   Significant wave height (proportional to length of bars) and mean propagation direction (indicated by direction of bars) of principal partitioned wave systems for WAM (panel a) and SAR derived wave spectra (panel b).
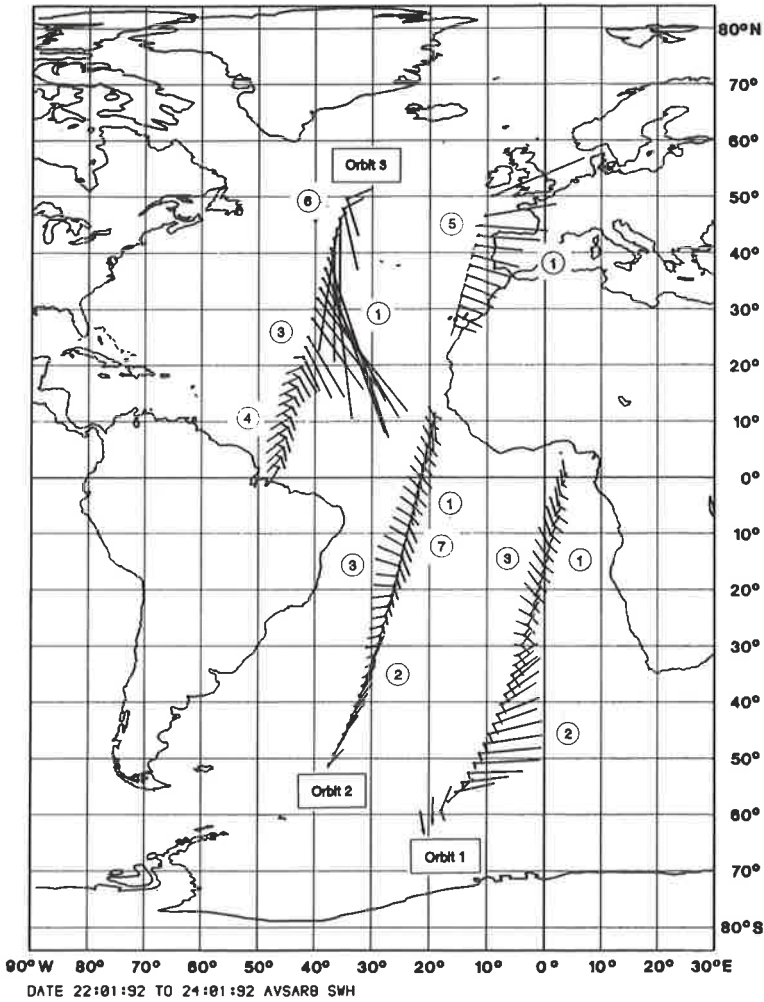
ERS1 WAVE MODE

FIGURE 18   (*Continued*)

8. CONCLUSIONS

From a first evaluation of the ERS-1 SAR wave mode data collected over the Atlantic during the three-day period 22–24 January, 1992, the following conclusions may be drawn:

(1) Nearly all of the imagettes were of high quality and exhibited a variety of wave systems traveling in both range and azimuthal direction. Of the 494 wave imagettes received within the WAM wave model domain, five were rejected because of low

signal-to-noise ratios (ratio of peak energy density of the imagette spectrum to background clutter noise level less than 3 dB), and four because the wave heights of the first-guess model wave spectrum were extremely low (less than 0.5 m).

(2) Of the remaining quality-controlled 485 imagette spectra, 467 could be success-fully inverted using the HH technique, yielding realistic looking wave spectra. In the eighteen cases which failed to converge, the SAR spectra exhibited pronounced non-wave-like features, usually at long wavelengths, which were presumably associated with other surface phenomena such as slicks or wind rows. For the successful inversions, the SAR spectra, after corresponding to the optimally fitted wave spectra,
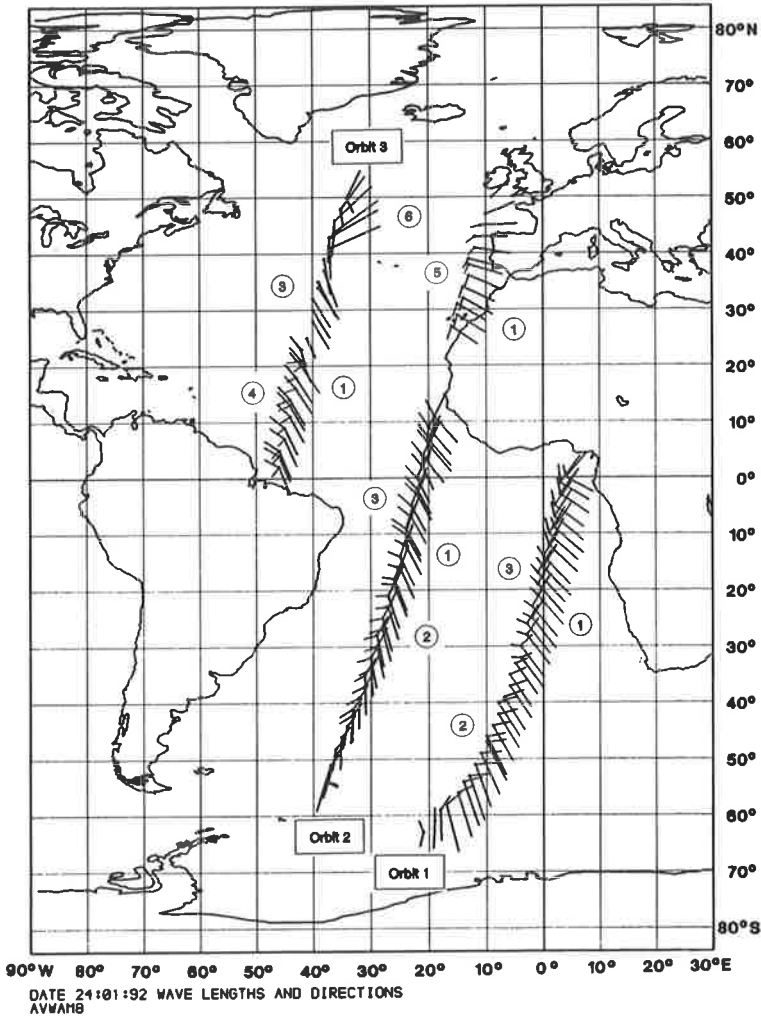

FIGURE 19   Same as Figure 18, but for mean wavelength instead of significant wave height.
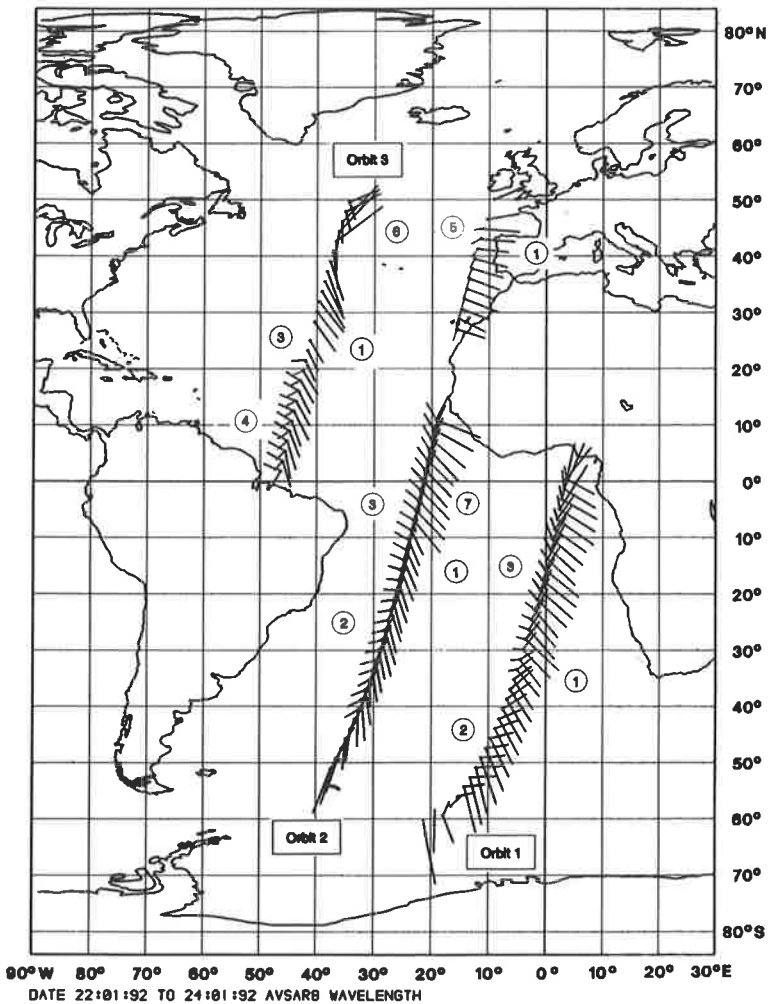
ERS1   WAVE MODE

FIGURE 19   (Continued)

were in very close agreement with the observed SAR spectra, and the optimally fitted wave spectra were relatively insensitive to the precise form of the input first-guess wave spectrum—as expected and required for a reliable inversion scheme. The impact from the first-guess wave spectrum is relevant mainly for resolving the 180° directional ambiguity of the SAR and for augmenting the spectrum at wavenumbers beyond the approximately 100–200 m azimuthal cut-off of the SAR.

(3) The overall agreement between the SAR-retrieved wave spectra and the first-guess wave spectra computed with the WAModel was good, thereby jointly validating both the ERS-1 SAR wave mode and the WAModel. The agreement holds not only for
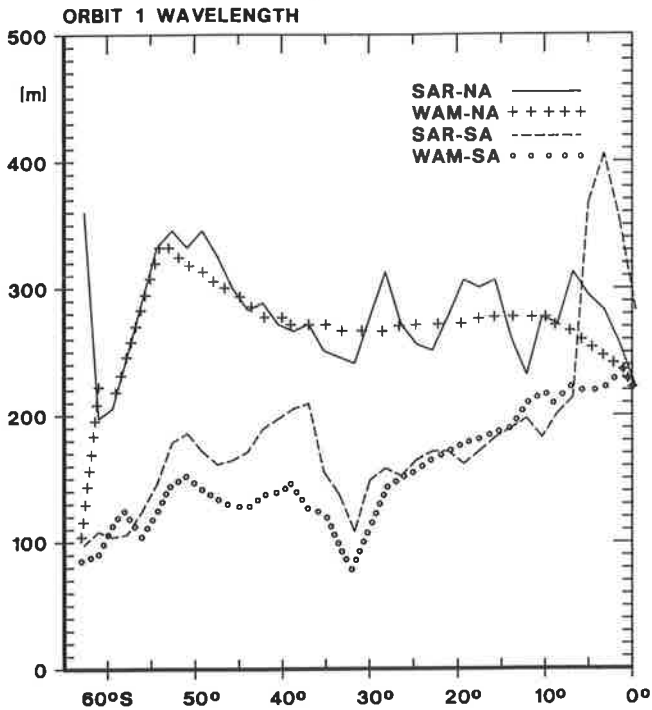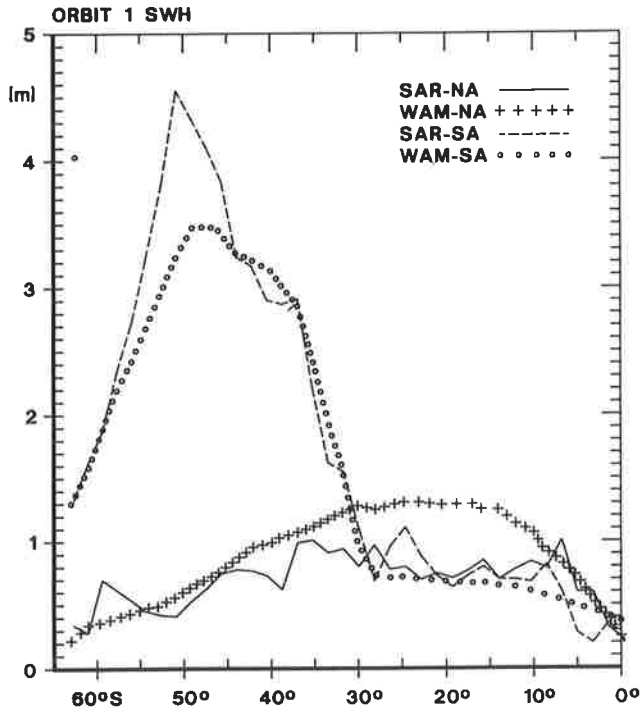
FIGURE 20 Intercomparison of wave heights (panel a) and wavelengths (panel b) of wave system 1 (North Atlantic system) and 2 (South Atlantic system) along orbits 1 and 2 in the South Atlantic.
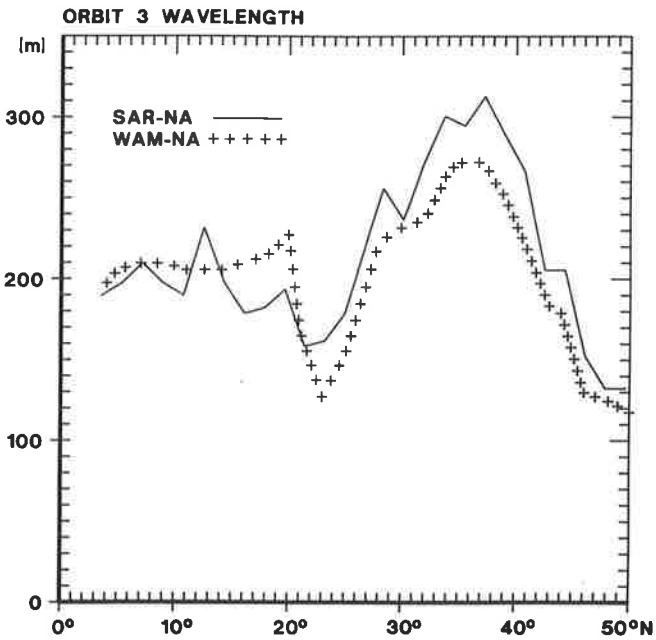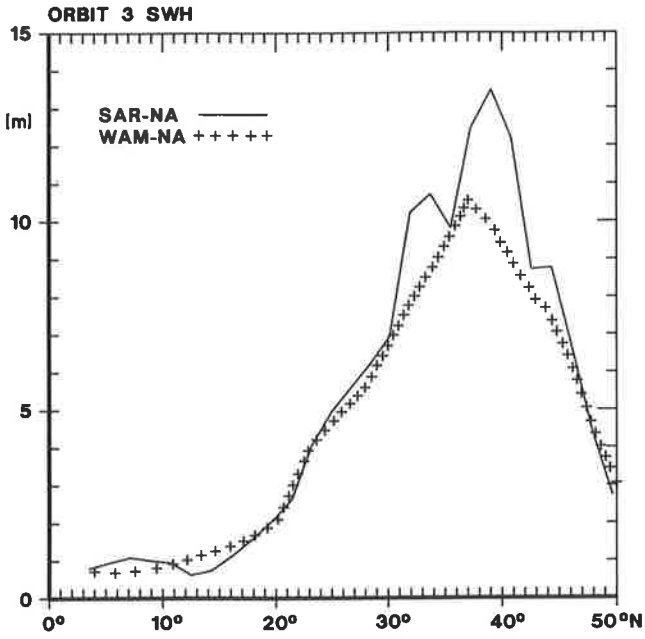
FIGURE 21 Intercomparison of wave heights (panel a) and wavelengths (panel b) of wave system 1 (North Atlantic system) along orbit 3 in the North Atlantic.

mean spectral parameters such as the significant wave height, mean propagation direction, mean wavelength and directional spread, but also for the individual wave systems characterizing the rather complex wave spectra which are typically found in the open Atlantic. The SAR wave height measurments (which were calibrated by the measured clutter spectra, independently of the SAR instrument calibration) exhibit an accuracy of the order of 10%, comparable to the accuracy of radar altimeter wave height measurements. However, for waves higher than about 5 m the SAR wave heights tend to exceed the modeled wave heights by approximately 15%. Problems identified were related to the different clutter cut-off wavelengths of the observed and simulated SAR image spectra. An improved inversion algorithm is currently being developed to resolve these deficiencies.

(4) Despite the good overall agreement, discrepancies are nevertheless found for individual wave systems. These may indicate deficiencies in the wind field, the wave model or in the SAR mapping theory. The statistical basis of the present data set is insufficient to decide clearly between these alternatives, but it appears likely that while all three contribute to the error balance to some degree, the wind fields represent the most significant source of error. Wind field errors are expected to be greatest in the South Atlantic, where direct wind measurements are relatively sparse (this is supported by the more extensive six-month global analysis of ERS-1 SAR wave mode data of Brüning et al., 1993). Systematic errors of the WAModel have been difficult to detect in the past on the basis of existing wave data (the few reliable data were used to tune the model), but the continuously growing global data base of two-dimensional directional spectra retrieved from ERS-1 SAR wave mode data should now provide a unique data base for wave model testing. Finally, individual intercomparisons of modeled and observed SAR spectra suggest that the representation of the hydro-dynamic modulation transfer function, the weakest element of the SAR mapping theory which mainly affects range traveling waves, should be improved. This should also be now possible by systematic tuning of the SAR imaging model against the expanding global ERS-1 SAR wave mode data base.

In summary, a first preliminary analysis of only three days of ERS-1 SAR wave mode data restricted to the Atlantic Ocean indicates that the instrument is functioning exceptionally well and providing quantiative global wave spectral data which should prove invaluable for the improvement of wind and wave forecasting when assimilated into wind and wave models.

APPENDIX: CLUTTER NOISE LEVEL FOR AMPLITUDE-AVERAGED MULTI-LOOK IMAGES

Relation between Energy and Amplitude Averaged Multi-look Images

SAR spectra of ocean wave images are unavoidably contaminated by clutter noise arising from the Gaussian statistics of the return signals from individual backscattering elements of the random sea surface. Since the backscattered returns from different backscattering elements are statistically uncorrelated, the clutter noise spectrum is essentially white. (The decorrelation is caused by the independent random phases of the

backscattered signals; although the signals are correlated in amplitude through the long-wave modulation, this mechanism does not produce a correlation of the complex signals if the phases are random). Consideration of the antenna pattern leads to gradual cut-off of the white clutter spectrum at high wavenumbers, but this is not relevant for the present analysis.

The background clutter noise spectrum limits the high wavenumber resolution of the spectrum, since the signal spectrum due to the long-wave modulation can no longer be determined when it falls below the level of the clutter spectrum (Alpers and Hassel-mann, 1982, referred to hereafter as AH). However, the existence of a clutter noise background also has a great advantage: it provides natural calibration of the SAR ocean wave image spectrum independent of the SAR instrument calibration. For a Gaussian backscattering surface, the variance of the backscatter return of an individual backscattering element is equal to the square of the mean backscattering return. Thus the background clutter spectrum is proportional to the square of the mean cross-section. Since the spectral ocean wave signal is determined by processes modulating the mean backscatter cross-section, it is also measured in units of the mean cross-section squared. Thus the ratio of the ocean wave spectrum to the clutter background noise spectrum is independent of the absolute SAR calibration or mean cross-section: it is determined only by the (well-defined) geometrical size of the SAR resolution pixel, which determines the spectral extent of the background clutter spectrum, and the wave modulation factors, which one wishes to measure.

These relations were derived in some detail in AH, including the influence of the SAR antenna pattern and the instrument response which determine the pixel geometry and the high wavenumber fall-off of the clutter spectrum. For application to the ERS-1 SAR, however, the analysis of AH has to be slightly modified. The authors assumed that the SAR multi-look image was formed by averaging the energies (i.e. measured cross-sections σ_i) over n looks. In the ERS-1 SAR, however, the multi-look image is formed by averaging over the amplitudes $a_i = \sqrt{\sigma_i}$ and then subsequently squaring the average. This yields a slightly different ratio of the clutter variance to the square of the mean cross-section, as shown below.

Ignoring antenna pattern effects, it can be assumed that the derivations σ_i' of the measured cross-sections of individual looks from the expectation value $\langle \sigma_i \rangle = \sigma_0$ are statistically independent:

$$\sigma_i = \sigma_0 + \sigma_i' \tag{A1}$$

where for a Gaussian backscattering surface

$$\langle \sigma_i' \sigma_j' \rangle = \delta_{ij} \sigma_0^2 \tag{A2}$$

(cornered parentheses $\langle \cdots \rangle$ denote ensemble means).

Other moments will also be needed in the following. For a Gaussian backscattering surface, the probability distribution $p(a)$ of the amplitudes $a_i = \sqrt{\sigma_i}$ of the backscatter return of a single look is given by the Rayleigh distribution,

$$p(a) = (2/\sigma_0) a \exp(-a^2/\sigma_0). \tag{A3}$$

This yields generally for the n'th moment

$$a_n = \langle a^n \rangle = (\sigma_0)^{n/2} \Gamma(n/2 + 1) \tag{A4}$$

and in particular for the first four moments

$$a_1 = \langle a \rangle = (\sqrt{\pi/4}) \cdot \sqrt{\sigma_0} \tag{A5}$$

$$a_2 = \langle a^2 \rangle = \sigma_0 \tag{A6}$$

$$a_3 = \langle a^3 \rangle = \left(\frac{3}{4}\right) \sqrt{\pi} (\sigma_0)^{3/2} \tag{A7}$$

$$a_4 = \langle a^4 \rangle = 2\sigma_0^2 \tag{A8}$$

(The index i is dropped here and in the following when it is clear that the ensemble of individual single-look realizations of the backscatter from a given elementary resolution cell is being considered.)

Equation (A2) follows then from (A6) and (A8):

$$\langle (\sigma')^2 \rangle = \langle (a^2 - \langle a^2 \rangle)^2 \rangle = \langle a^4 \rangle - \langle a^2 \rangle^2 = \sigma_0^2. \tag{A9}$$

In AH, the multi-look average cross-section was defined as the mean of the single-look energies (cross-sections)

$$\bar{\sigma}_e = \frac{1}{n} \sum_i \sigma_i \tag{A10}$$

while for ERS-1 the corresponding expression is defined as the square of the mean amplitudes

$$\bar{\sigma}_a = \left(\frac{1}{n} \sum_i a_i\right)^2 = (\bar{a})^2. \tag{A11}$$

The clutter noise variance $N = N_e$ of N_a is defined in both cases as

$$N = \langle \delta \bar{\sigma}^2 \rangle = \langle (\bar{\sigma} - \langle \bar{\sigma} \rangle)^2 \rangle. \tag{A12}$$

For both forms of averaging, the clutter noise variance determines the level of the background clutter spectrum $F_{cl}(k)$. Since the clutter noise variations of $\bar{\sigma}$ for different backscattering cells are statistically independent, $F_{cl}(k)$ is white (ignoring the antenna pattern effects at high wavenumbers), and is therefore computed by simply distributing the total variance N uniformly over the wavenumbers of the (two-sided) two-dimensional spectrum between the limiting negative and positive Nyquist cut-off wavenumbers

$$k_x^{Nyq} = \pm \frac{1}{(2\Delta x)}, \quad k_y^{Nyq} = \pm \frac{1}{(2\Delta y)}, \quad \text{where } \Delta x, \Delta y, \text{ is the pixel size:}$$

$$F_{cl}(k) = N \Delta x \Delta y. \tag{A13}$$

For the application of the results of AH to ERS-1 we need to determine only the ratio of N_e (computed by AH) to N_a (the relevant quantity for ERS-1).

Computation of N_e and N_a

The energy-averaged multi-look clutter noise is given by the variance

$$N_e = \langle \delta\sigma_e^2 \rangle = \left\langle \left[\frac{1}{n} \sum_i (\sigma_i - \sigma_0) \right]^2 \right\rangle = \left\langle \left[\frac{1}{n} \sum_i \sigma_i' \right]^2 \right\rangle = \frac{1}{n} \sum_i \langle \sigma_i'^2 \rangle \qquad \text{(A14)}$$

or, from equation (A2)

$$N_e = \frac{1}{n} \sigma_0^2. \qquad \text{(A15)}$$

The corresponding expression for the amplitude averaged multi-look clutter variance is given by

$$N_a = \langle \delta\sigma_a^2 \rangle = \left\langle \left[\left(\frac{1}{n} \sum_i a_i \right)^2 - \left\langle \left(\frac{1}{n} \sum_i a_i \right)^2 \right\rangle \right]^2 \right\rangle$$

$$= n^{-4} \left\langle \left[\sum_{i,j} a_i a_j - \left\langle \sum_{i,j} a_i a_j \right\rangle \right]^2 \right\rangle$$

$$= n^{-4} \sum_{i,j,k,l} Q_{ijkl} \qquad \text{(A16)}$$

where

$$Q_{ijkl} = \langle a_i a_j a_k a_l \rangle - \langle a_i a_j \rangle \langle a_k a_l \rangle. \qquad \text{(A17)}$$

In carrying out the sums over i, j, k, l we can distinguish between the following index combinations:

(i) all i, j, k, l are different

$$Q_{ijkl} = \langle a \rangle^4 - \langle a \rangle^4 = a_1^4 - a_1^4 = 0 \qquad \text{(A18)}$$

(ii) three different indices, one equal-index pair, with (first combination)

$$i = j \text{ and } i, k, l \text{ all different or}$$

$$k = l \text{ and } k, i, j \text{ all different}$$

$$Q_{ijkl} = a_2 a_1^2 - a_2 a_1^2 = 0 \qquad \text{(A19)}$$

or

(iii) three different indices, one equal-index pair, with (second combination)

$$i = k \text{ and } i, j, l \text{ all different or}$$

$$j = k \text{ and } j, i, l \text{ all different or}$$

the same two combinations with k and l interchanged

$$Q_{ijkl} = a_2 a_1^2 - a_1^4 \qquad \text{(A20)}$$

total number of terms: $4n(n-1)(n-2)$

(iv) two different equal-index pairs of indices, with (first combination)

$$i = j, \quad k = l, \quad i \neq k:$$

$$Q_{ijkl} = a_2^2 - a_2^2 = 0 \tag{A21}$$

or

(v) two different equal-index pairs of indices, with (second combination)

$$i = k, \quad j = l, \quad i \neq j \quad \text{or}$$

$$i = l, \quad j = k, \quad i \neq j:$$

$$Q_{ijkl} = a_2^2 - a_1^4 \tag{A22}$$

total number of terms: $2n(n-1)$

(vi) three equal indices, one different

$$Q_{ijkl} = a_3 a_1 - a_2 a_1^2 \tag{A23}$$

number of terms: $4n(n-1)$

(vii) four equal indices

$$Q_{ijkl} = a_4 - a_2^2 \tag{A24}$$

number of terms: n

Collecting all expressions we obtain

$$N_a = n^{-3}[a_4 + 4(n-1)a_3 a_1 + (2n-3)a_2^2$$
$$+ 4(n-1)(n-3)a_2 a_1^2 - 2(n-1)(2n-3)a_1^4 \tag{A25}$$

For ERS-1, $n = 3$, this yields

$$N_a = \frac{1}{27}[a_4 + 8a_3 a_1 + 3a_2^2 - 12a_1^4] \tag{A26}$$

or, invoking equations (A5)–(A8)

$$N_a = \sigma_0^2 \frac{1}{27}\left(5 + 3\pi - \frac{3}{4}\pi^2\right) \tag{A27}$$

yielding

$$N_a = 0.26\,\sigma_0^2 \tag{A28}$$

The corresponding expression (A14) for the energy averaged multi-look clutter noise yields for $n = 3$

$$N_a = \frac{1}{3}\sigma_0^2 \tag{A29}$$

so that for ERS-1

$$\frac{N_a}{N_e} = (0.26)(3) = 0.78 \tag{A30}$$

References

Alpers, W. and Hasselmann, K. (1978) The two-frequency technique for measuring ocean wave spectra from an airplane or satellite. *Boundary Layer Meteorol.*, **13**, 215–230.

Alpers, W., Ross, D.B. and Rufenach C.L. (1981) On the detectability of ocean surface waves by real and synthetic aperture radar. *J. Geophys. Res.*, **86**, 5481–6498.

Alpers, W. and Hasselmann, (1982) Spectral signal to clutter and thermal noise properties of ocean wave imaging synthetic aperture radars. *Int. J. Remote Sens.*, **3**, 423–446.

Alpers, W., Brüning, C. and Richter, K. (1986) Comparison of simulated and measured synthetic aperture radar image spectra with buoy-derived ocean wave spectra during the Shuttle Imaging Radar B mission, *IEEE Trans. Geosci. Remote Sens.*, GE-24, 559–566.

Alpers, W. and Brüning, C. (1986) On the relative importance of motion-related contributions to the SAR imaging of ocean surface waves. *IEEE Trans. Geosci. Remote Sens.*, GE-24, 873–885.

Bao, M., Brüning, C. and Alpers, W. (1994) A generalized nonlinear spectral integral transform and its application to ERS-1 SAR ocean wave imaging, to be published in Proc. of the second ERS-1 symposium, Hamburg, Oct. 11–14, 1993. ESA publication.

Bauer, E., Hasselmann, S., Hasselmann, K. and Graber, H.C. (1992) Validation and assimilation of Seasat alimeter wave heights using the WAM wave model. *J. Geophys. Res.*, **97**, 12671–12682.

Brüning, C., Alpers, W. Zambresky, L.F. and Tilley, D.G. (1988) Validation of a synthetic aperture radar ocean wave imaging theory by the Shuttle Imaging Radar-B experiment over the North Sea. *J. Geophys. Res.*, **93**, 15403–15425.

Brüning, C., Alpers, W. and Hasselmann, K. (1990) Monte-Carlo simulation studies of the nonlinear imaging of a two dimensional surface wave field by a synthetic aperture radar. *Int. J. Remost Sens.*, **11** (10), 1695–1727.

Brüning, C., Alpers, W. and Wilde, (1992) Ocean wave imaging by ERS-1 synthetic aperture radar: First results from the Haltenbanken Calibration/Validation campaign, Proc. of the ERS-1 Geophysical Validation Workshop, Penhors, Bretagne, France, 27–20 April, 1992. ESA Publication.

Brüning, C., Hasselmann, S., Hasselmann, K., Lehner, S. and Gerling, T. (1993) On the extraction of ocean wave spectra from ERS-1 SAR wave mode image spectra. In Proc. of the first ERS-1 symposium, Cannes, Nov. 2–4, 1992, ESA publication.

Brüning, C. (1994) On the relative importance of the ocean wave-radar modulation transfer function for inverting ERS-1 SAR image spectra into ocean wave spectra, to be published in Proc. of the second ERS-1 symposium, Hamburg, Oct. 11–14, ESA publication, 1994.

Gerling, T. (1992) Partitioning sequences and arrays of directional ocean wave spectra into component wave systems. *Journal of Atmospheric and Oceanic Technology*, Vol. 9, No. 4, 444–458.

Gower, J.F.R. (1983) Layover in satellite radar images of ocean waves. *J. Geophys. Res.*, **88**, 7719–7720.

Günther, H., Hasselmann, S. and Janssen, A.E.M. (1992) Wamodel Cycle 4, Deutsches Klimarechenzentrum, Hamburg, Technical Report No. 4.

Hara, T. and Plant, W. J. (1993) Hydrodynamic modulation of short wind-wave spectra due to long waves measured by microwave radar, submitted to *J. Geophys. Res.*,

Hasselmann, K. et al. (1985) Theory of a synthetic aperture radar ocean imaging. A MARSEN view. *J. Geophys. Res.*, **90**, 4659–4686.

Hasselmann, K., Hasselmann, S., Brüning, C. and Speidel, A. (1991) Interpretation and application of SAR wave image spectra in wave models. In R.C. Beal (ed.) *Directional Ocean Wave Spectra*, Baltimore: The Johns Hopkins University Press.

Hasselmann, K. and Hasselmann, S. (1991) On the nonlinear mapping of an ocean wave spectrum into a SAR image spectrum and its inversion. *J. Geophys. Res.*, **96**, C6, 10713–10729.

Hasselmann, S., Brüning, C. and Lionello, P. (1994a) Towards a generalized optimal interpolation method for the assimilation of ERS-1 SAR retrieved wave spectra in a wave model, to be publised in Proc. of the ERS-1 symposium, Hamburg, Oct. 11–14, 1993, ESA publication.

Hasselmann, S., Hasselmann, K. and Brüning, C. (1994b) Extraction of wave data from ERS-1 SAR wave mode spectra, to be published in Proc. of the second ERS-1 symposium, Hamburg, Oct. 11–14, 1993. ESA publication.

Hansen, B., Brüning, C. and Staabs, C. (1994) Global comparison of significant wave heights derived from ERS-1 SAR wave mode, ERS-1 altimeter and TOPEX altimeter data, to be published in Proc. of the second ERS-1 symposium, Hamburg, Oct. 11–14, 1993, ESA publication.

Krogstad, H.E. (1992) A simple derivation of Hasselmann's non-linear ocean-synthetic aperture radar transform. *J. Geophys. Res.*, **97**, 2421–2425.

Larson, T.R., Moskowitz, L.I. and Wright, J.W. (1976) A note on SAR imager of the ocean. *IEEE Trans. Antennas Propagat.* Ap-24, 393–394.

Plant, W.J., Keller, W.C. and Cross, A. (1983) Parametric dependence of ocean waveradar mudulation transfer functions, *J. Geophys. Res.*, **88**, 9747–9756.

Rosenthal, W., Ziemer, F. Raney, K. Vachon, P. (1989) Removal of 180° ambiguity in SAR images of ocean waves. Paper presented at IGARSS '89, Remote Sensing: An Economic Tool for the Nineties, Vancouver, Canada, July 10–14.

Snodgrass, F.E., Groves, G.W., Hasselmann, K.F., Miller, G.R., Munk, W.H. and Powers, W.H. (1966) Propagation of ocean swell across the Pacific. *Phil. Trans. R. Soc.*, (A) **259**, 431.

Swift, C.T. and Wilson, L.R. (1979) Synthetic aperture radar imaging of ocean waves. *IEEE Trans. Antennas Propagat.* Ap-27, 725–729.

Vachon, P.W. and Raney, R.K. (1989) Resolution of ocean wave propagation direction in single-pass airborne SAR imagery. Proc. IGARSS '89, Vancouver, Canada.

WAMDIG: The WAM-Develoment and Implementation Group, Hasselmann S., Hasselmann, K., Bauer, E., Bertotti, L., Cardone, C.V. Ewing, J.A. Green-wood, J.A., Guillaume, A. Janssen, P.AE.M., Komen, G.J. Lionello, Reistad, M. and Zambresky, L. (1988) The WAM Model—a third generation ocean wave prediction model. *J. Phys. Oceanogr.*, **18**, 12, 1775–1810.

Wilde, A. et al. (1994) Comparison of ocean wave imaging by ERS-1 and ALMAZ-1 synthetic aperture radar, to be published in Proc. of the second ERS-1 symposium, Hamburg, Oct. 11–14, 1993. ESA publication.

Yamartino, R.J. (1984) A comparison of several 'single-pass' estimators of the standard deviation of wind direction. *J. Climate Appl. Meteor.*, **23**, 1362–1366.